HHS Public Access

Author manuscript

Int J Coal Geol. Author manuscript; available in PMC 2015 September 30.

Published in final edited form as:

Int J Coal Geol. 2012 February 1; 90-91: 50–71. doi:10.1016/j.coal.2011.10.010.

Geostatistical modeling of the gas emission zone and its in-place gas content for Pittsburgh-seam mines using sequential Gaussian simulation

C. Özgen Karacan[a,*], **Ricardo A. Olea**[b], and **Gerrit Goodman**[a]

[a]NIOSH, Office of Mine Safety and Health Research, Pittsburgh, PA, United States

[b]USGS, Eastern Energy Resources, Reston, VA, United States

Abstract

Determination of the size of the gas emission zone, the locations of gas sources within, and especially the amount of gas retained in those zones is one of the most important steps for designing a successful methane control strategy and an efficient ventilation system in longwall coal mining. The formation of the gas emission zone and the potential amount of gas-in-place (GIP) that might be available for migration into a mine are factors of local geology and rock properties that usually show spatial variability in continuity and may also show geometric anisotropy. Geostatistical methods are used here for modeling and prediction of gas amounts and for assessing their associated uncertainty in gas emission zones of longwall mines for methane control.

This study used core data obtained from 276 vertical exploration boreholes drilled from the surface to the bottom of the Pittsburgh coal seam in a mining district in the Northern Appalachian basin. After identifying important coal and non-coal layers for the gas emission zone, univariate statistical and semivariogram analyses were conducted for data from different formations to define the distribution and continuity of various attributes. Sequential simulations performed stochastic assessment of these attributes, such as gas content, strata thickness, and strata displacement. These analyses were followed by calculations of gas-in-place and their uncertainties in the Pittsburgh seam caved zone and fractured zone of longwall mines in this mining district. Grid blanking was used to isolate the volume over the actual panels from the entire modeled district and to calculate gas amounts that were directly related to the emissions in longwall mines.

Results indicated that gas-in-place in the Pittsburgh seam, in the caved zone and in the fractured zone, as well as displacements in major rock units, showed spatial correlations that could be modeled and estimated using geostatistical methods. This study showed that GIP volumes may change up to 3 MMscf per acre and, in a multi-panel district, may total 9 Bcf of methane within the gas emission zone. Therefore, ventilation and gas capture systems should be designed accordingly. In addition, rock displacements within the gas emission zone are spatially distributed.

*Corresponding author. Tel.: +1 412 386 4008. cok6@cdc.gov (C.Ö. Karacan).

Disclaimer: The findings and conclusions in this paper are those of the authors and do not necessarily represent the views of the National Institute for Occupational Safety and Health or of USGS. Mention of any company name, product, or software mentioned in this paper does not constitute endorsed by NIOSH or USGS.

From an engineering and practical point of view, spatial distributions of GIP and distributions of rock displacements should be correlated with in-mine emissions and gob gas venthole productions.

Keywords

Geostatistical modeling; Sequential Gaussian simulation; Northern Appalachian Basin; Gas emission zone; Methane emission; Longwall mining

1. Introduction

Drilling vertical gob gas ventholes (GGVs) from the surface ahead of mining is a common technique used in the U.S. to capture methane emissions within the overlying fractured strata before this gas enters the work environment. Cross-measure boreholes are drilled using various design principles for the purpose of draining roof and floor rock strata as they relax during mining. In Europe, due to the greater depths of the longwall mines, cross-measure boreholes are preferred over GGVs. For each of these methane control measures, placement of boreholes and operational parameters play important roles in controlling methane emissions before they enter the working space (Karacan, 2009a; Karacan and Luxbacher, 2010; Karacan et al., 2011).

In addition to controllable factors such as borehole placement and operational parameters, reservoir and geomechanical characteristics of the overlying (and in some cases underlying) strata that are affected by mining disturbances can control both the productivity and stability of these boreholes (Karacan et al., 2011; Whittles et al., 2006, 2007). This zone of deformation, known as the “gas emission zone” of a longwall mine, hosts the sources of longwall gas providing gas to the boreholes, leads to in-mine emissions (Karacan and Goodman, 2011a; Noack, 1998; Thakur, 2006), and interferes with the stability of boreholes.

Existing and mining-induced fractures may expand within the gas emission zone as a consequence of the mining. The generation and propagation of the fractures depend on the type and composition of the rocks overlying the mined seam. Methane emissions can occur as sudden and unstable releases, provided that there is enough gas contained within the emission zone sources. This can lead to potentially dangerous underground conditions if not prevented with a properly designed ventilation system or with effective gas capture measures.

Fractures and methane emissions above a coal mine are closely related to the geology of coal and coal-measure rocks, their properties, and their distances from mining activity. However, there must be sufficient gas within the gas emission zone, in combination with strata deformation, to create a threat to mining safety. The common gas sources in the overlying formations are caved or fractured coal seams. Strata below the mined seam may also be a major gas source if they contain gassy seams or gassy sandstones.

Three important considerations are necessary in order to make an assessment of gas emissions: a) the ability to predict the size of the gas emission zone, b) knowledge of the properties of coal seams and rock layers, and c) how much gas these strata contain within

the gas emission zone. This information can help in predicting the likelihood of sudden gas releases and changes in emission rates, as well as in designing surface methane control systems.

Different researchers have described gas emission zone sizes and emission potentials at various heights above the coal seam (Noack, 1998; Thakur, 2006). These studies show the degree of gas emissions as a function of varying distances from the mined coal bed in overlying and underlying formations. Considering that there is always some uncertainty associated with overlying and underlying formations and with how they may react to mining disturbances, a site-specific and probabilistic approach to define the gas emission zone is always better for estimating and controlling emissions. Karacan and Goodman (2011a) have conducted a probabilistic study for a mining district in Southwestern Pennsylvania in the Northern Appalachian basin based on the displacements measured in GGVs to define the size of the gas emission zone during mining of the Pittsburgh coal seam. This study showed that the deformed zone may extend as high as 350–100 ft above the Pittsburgh seam, and that the probability of obtaining specific strata displacements may vary based on the proximity of the formation to the Pittsburgh seam, although it did not consider spatial distribution due to lack of sufficient data. In all studies exploring the gas emission zone and its size, three major zones were considered: a caved zone, a highly fractured zone, and a composite beam zone. These zones are important for gas emissions and transport into the mining environment, provided that there are sources with high methane amounts within these intervals.

Even if the size (height) of the gas emission zone can be estimated globally using various methods or assumptions, it is not uncommon that gas emission predictions may be under- or over-estimated due to the lack of sufficient spatial information defining the quantity and location of the gas sources in the overlying strata. Core analyses and geophysical logging techniques are two of the important data sources for characterizing the geological formations and their gas contents in the gas emission zone (Karacan and Diamond, 2006). Determinations of reservoir and geomechanical properties of the formations are important because they affect fluid flow and storage in the overburden before and after coal extraction, with the stress and strain states changing as a result of longwall operations. Thus, laboratory analyses of available core materials from boreholes and accurate borehole logs of coal measure rocks are necessary for any emission prediction (Karacan, 2009b). However, laboratory analysis on cores of sampled locations, although beneficial, provides data only from point locations. This method provides data that are non-continuous and also does not specify a sampling count or spacing of the data, with the goal of obtaining a continuous picture of a geological attributes in the gas emission zone of a continuous operation, i.e. longwall mining. Even if the mining area is drilled by exploration boreholes for exhaustive sampling of cores, at the expense of cost and time, the data in intervening spaces is unknown. In this regard, geostatistics and geostatistical modeling are unique methods to establish spatial correlations in sampled data to form continuity, to enable precision, and to assess the uncertainty of the attributes that are being investigated (e.g. Webster and Oliver, 2009).

Geostatistical analyses and modeling techniques, some of which are described in detail in Deutsch and Journel (1998), Olea (2009), Remy et al. (2009), and Wackernagel (2010), have been widely used for geological, environmental, mining, and petroleum engineering. For instance, Hohn and Neal (1986) used geostatistical analysis to estimate the gas potential in Devonian shales of West Virginia. Watson et al. (2001) used a geostatistical approach to predict sulfur content in the Pittsburgh coal seam. Olea et al. (2011) presented a methodology using geostatistical approaches to quantify the uncertainty in coal resource assessments, applying the technique to a Texas lignite deposit. Heriawan and Koike (2008) identified spatial heterogeneity and resource quality of a coal deposit in Indonesia using geostatistics. They also correlated the distribution of various elements within the coal using multivariate geostatistics. Hindistan et al. (2010) used kriging as a tool to predict and control coal quality during longwall mining so that produced coal would comply with certain product specifications. Falivene et al. (2007) used geostatistical techniques to develop optimum and robust interpolation strategies in a heterogeneous coal zone in Spain. They concluded that optimum gridding, spatial correlation, and modeling can generate more accurate and realistic fades and coal property reconstructions. In addition to coal research, geostatistics have been used to assess spatial uncertainty of soil water content (Delbari et al., 2009), to explore the spatial relations between soil physical properties and electrical conductivity (Carroll and Oliver, 2005), and to conduct spatial analyses of metal contents in sediments of the Yangtze River basin (Zhang and Selinus, 1997).

These studies are only selected examples and there are many others in the literature that document the use of different geostatistical techniques, such as semivariogram analyses, kriging, and stochastic simulation methods, on spatially correlated data in various disciplines related to the earth sciences. Geostatistics can be used to account for a wide range of data of varying resolutions, quality, and uncertainty for reconciling data types at different scales and for constructing models of geological heterogeneity (Leuangthong et al., 2008). These data and models can later be used as inputs for solving dynamic problems such as flow models.

Section contains a list of abbreviations and unit conversion factors.

1.1. Statement of problem

This paper quantifies gas-in-place, its uncertainty, and the displacements of major non-coal layers in the gas emission zones of longwall mines in a mining district in the Northern Appalachian Basin. These analyses will lead to improved design and application of methane capture and control systems.

In this study, the probabilistic gas emission zone prediction method presented in Karacan and Goodman (2011a) was combined with core data, including thickness and depth of major coal and non-coal formations, obtained from 276 exploration boreholes. Semivariogram analyses followed by sequential simulations were conducted to predict displacements in major non-coal layers and to predict gas-in-place in coals on a district-wide scale (in MMscf). Gas amounts were later specifically computed for a mined coal seam (Pittsburgh coal), in the caved zone, and in the fractured zone of the longwalls.

The results of simulations will be emphasized and analyzed in the Results and discussion section, although both kriging and simulations were performed and their results compared for variances and distributions. This preference is due to the inherent differences between these two techniques. Simulation differs from kriging in its superior ability to reproduce patterns of spatial continuity and produce realistic uncertainty modeling. Although there are no clear rules to exclude either kriging or simulation from a geostatistical analysis (Olea, 2009), kriging is recommended if the ultimate criterion is individual minimization of prediction error or the development of a smooth exploratory mapping of an unknown attribute. However, if the main objective is the correct assessment of confidence intervals or the correct modeling of spatial continuity, then simulation is the appropriate tool (Olea, 2009). Therefore, sequential Gaussian simulation was used as the preferred analysis technique in this study.

The geostatistical analyses used in this work gave not only the spatial correlations of thickness and gas content of coals (in scf/ton) that were used to calculate gas-in-place, but also enabled uncertainty analyses using the results of realizations at 5%, 50%, and 95% quantiles. Furthermore, grid blanking was used to isolate the volumes over the actual panels from the entire district to calculate gas-in-place and regions of higher rock displacement.

2. Studied mining district and its geology that is important for the gas emission zone

2.1. Coal seams as methane sources and major non-coal strata within the gas emission zone of longwall mines in the studied district

The studied longwall mining district is located in the southwestern Pennsylvania (in Greene County) section of the Northern Appalachian Basin (Fig. 1). The southwestern Pennsylvania section of the basin is a very important area for coal mining and for coalbed and coal mine methane capture and production. Markowski (1998) reported that 11 of the 24 intervals with coalbed methane in Pennsylvania are located in Greene County, Pennsylvania. Due to extensive coal mining in this area, these 11 gassy intervals (mostly coals) are closely associated with the mines operating in different coal seams and with their gas emission zones. Thus, these 11 coal intervals are potentially the major contributors to emissions in these mines.

The Monongahela Group of formations is within the gas emission zone when mining the Pittsburgh coal seam (Karacan, 2009b; Karacan and Goodman, 2011a). There are five main coals in the Monongahela Group of coal measures: the Pittsburgh coals, Redstone coal, Sewickley coal, Uniontown coal, and Waynesburg coals. The Pittsburgh coals consist of the main Pittsburgh seam and the Pittsburgh rider, which is usually located 1–3 ft above the Pittsburgh main coal. Overlying the Pittsburgh coal by 18–45 ft is the Redstone coal, which is not as extensive as the Pittsburgh. In general, the Redstone coal is 1–3 ft thick where present. The Sewickley coals include the Sewickley coal itself and any riders and splits of the main bench when it occurs. The deepest Sewickley coals are found in SW Pennsylvania at a depth of nearly 1170 ft. The Sewickley coal is laterally persistent and generally 1–6 ft thick. The Uniontown coal is not usually continuous, and when present, it is approximately

270–300 ft above the Pittsburgh coal with a thickness varying between 0.1 and 0.5 ft. The Waynesburg coals are made up of the Waynesburg coal, the Waynesburg A coal, and the Waynesburg B coal. The Waynesburg is laterally persistent and is usually multiple-bedded. These coal seams are shown in Fig. 1.

Pittsburgh coal is the main coal bed that is mined in the southwestern part of Pennsylvania. Due to their proximity to Pittsburgh coal, Pittsburgh riders and Redstone coals are usually within the caved volume and their gas is handled either by the ventilation system or by gob gas ventholes. Sewickley, Uniontown, and Waynesburg coals, on the other hand, are far enough from the Pittsburgh seam that they are part of the fractured section of the gas emission zone, as depicted in Fig. 1. These seams are believed to contribute to the gob gas in the fractured system (Karacan et al., 2007) and their gas emissions should be captured using gob gas ventholes.

Other non-coal formations of the Monongahela Group that do not contain significant amounts of gas but may affect caving and fracturing of the gas emission zone are shales of various kinds, limestones, and sandstones. These formations are inter-bedded with the coal seams and exist in varying thicknesses depending on the location. Based on the identifications given in the exploration boreholes, the thicknesses and their relatively high rock strengths compared to other strata, the Fishpot limestone, Sewickley sandstone, and Uniontown sandstone were selected for further geostatistical analyses (Fig. 1).

2.2. Setting of the mining district, mined panels, and general methane control

The mining district that was modeled in this work hosted panels N-1 through K (Fig. 2). This mining district was selected for study because mining was already completed in this area, because of data availability from the exploration boreholes and due to the previous reservoir modeling study detailed in Karacan et al. (2007), which evaluated the productions of gob gas ventholes in panels G to K and determined those factors affecting their performances. The dimensions of the area shown in Fig. 2 are 20,500 ft in the y-direction and 18,900 ft in the x-direction.

In this district, overburden depths ranged between 500 and 900 ft. Longwall panels in the primary area were initially 830 ft wide and were increased to 1000 ft starting with F Panel. Thus, the panels are super-critical—i.e., the panel width is greater than the depth of the overburden, which results in a more complete caving of the overburden strata into the mined void. Several coal seams presented in the previous section are within the gas emission zone of the longwall panels shown in Fig. 2, and are believed to be the primary source of caved and fractured strata gases in the area.

Methane control in the study longwall district included the bleeder ventilation system, gob gas ventholes, and underground horizontal methane drainage boreholes drilled prior to mining. The bleeder ventilation system included the peripheral bleeder entries surrounding the panels, the former gateroads between the mined-out panels, and the associated bleeder fan shaft(s). The bleeder fans operated in this district were located at the top of 6-ft-diameter air shafts. Gob gas ventholes of the panels in this mining area were generally drilled to

within 40–45 ft of the top of the Pittsburgh coal seam, cased with 7–8 in. of diameter pipe, and finished with 200 ft of slotted pipe on the bottom (Karacan et al., 2007).

Fig. 3 gives methane production rates from longwall bleeders of N–F panels (BF-2) and G–K panels (BF-3) during mining operation, with a missing period between the 300th and 700th days of mining. This figure also shows the methane production rates from gob gas ventholes drilled over these panels to remove gas from fractured strata. The data show that both bleeder rates and gob gas venthole rates differ between mining of these two panel districts. During mining of N–F panels, average methane production from GGVs is about 200 Mscfd, as opposed to 500–600 Mscfd from GGVs of G–K panels. This difference may be related to various factors discussed in Karacan (2009a) and differences in properties of the gob as a reservoir (Karacan, 2009c; Karacan and Goodman, 2011b). Similarly, methane rate from BF-2 averages around 2500–3000 Mscfd, where it is 1500–2000 Mscfd from BF-3. This may be related to the capacity of the bleeder fans. However, from both GGVs and bleeder fans, methane rates may be related to the availability of methane from various horizons and its spatial distribution as well, as explored in following sections.

3. Calculation of gas-in-place for coals within the gas emission zone and displacement of non-coal strata

In this study, the first objective was to quantify the gas amounts (gas-in-place) in various coal beds in the stratigraphic log shown in Fig. 1 and in the area shown in Fig. 2 using geostatistical methods. The second objective is to assess the gas amounts within the gas emission zone of panels N-1 to K. This section gives a brief overview of gas-in-place calculation prior to the geostatistical analyses. Gas content (gas amount per weight of coal) is one of the components of gas-in-place determination.

3.1. Gas content determination of coals

The gas content of coal can be measured or estimated using various techniques. These techniques usually fall into two categories: (1) direct methods which actually measure the volume of gas released from a coal sample (preferably wire line core samples) sealed in desorption canisters, and (2) indirect methods based on empirical correlations or laboratory-derived gas storage capacity data from sorption isotherms. An extensive review of direct techniques for gas content measurement for coal has been published by Diamond and Schatzel (1998). Properly conducted direct-method testing of coal cores provides relatively accurate estimates of in-place gas contents of coals for most mine planning purposes and allows for resource evaluation at a reasonably low cost. A modified direct method (MDM) procedure (Ulery and Hyman, 1991) provides an increased level of accuracy, but requires a higher level of instrumentation sophistication, procedural complexity, and cost.

Alternatively, regional gas content data on individual coal samples can be used along with auxiliary data on coal rank and/or depth to construct curves, as shown in Fig. 4, for estimating in-place gas contents for a specific area. Such curves are generated for a particular coal seam or closely associated group of coal beds and can be used to estimate gas content values only if the rank or depth is known for the coal bed of interest. The graph

given in Fig. 4 presents such curves for bituminous coals of the Black Warrior Basin, Alabama (McFall et al., 1986). However, in considering Fig. 4, it should be kept in mind that lithotype characteristics of coal also affect the methane content. Gas content generally varies positively with the amounts of vitrinite and liptinite, which usually offer high methane storage capacity. No obvious relationship is observed with inertinite content. Therefore, the smooth graphs in Fig. 4 should be interpreted and used with caution.

The geostatistical estimates of gas-in-place presented in this paper relate to coals of the Lower Monongahela Group. Site-specific information used to determine gas content of the coals and the gas content estimation technique were based on bivariate normal distributions presented in Karacan and Goodman (2011a).

In Karacan and Goodman (2011a), the gas contents of all seams given in Diamond et al. (1986) in Pennsylvania were compiled in a database, classifying all the coal beds above and including the Pittsburgh seam. Means (μ) and standard deviations (σ) of gas content and overburden depth for each coal studied in this work and the correlation coefficients (ρ) between variable pairs that were used in calculating joint probability distributions for gas content and depth are given in Table 1. All coals within the interval of interest in this study area are high volatile bituminous-A type coals with the gas content-depth relationship generally showing an increasing trend with depth. However, it should also be noted that gas contents show significant variations even at the same depth (Fig. 5) to establish a clear regression.

The bivariate normal probability calculations and representations of probabilities for obtaining gas contents less than or equal to 350 scf/ton with four-parameter logistic functions were used to estimate gas contents. These analyses showed that gas content of coals, most of which were from southwestern Pennsylvania, could be represented by the values of a dependent variable at 50% value of the independent variables (50% quantile—Q50) of these sigmoid functions, up to an overburden of 1400 ft. The polynomial representation of these coefficients gives a Pearson’s correlation coefficient of 0.9969 and is also given in Table 1. This relation was later used in this study to calculate the gas content of coals at Q50 as a function of depth.

Monte Carlo (MC) simulations were performed in order to determine similar relationships for 5% and 95% quantiles (Q5 and Q95) for each coal bed. These simulations were conducted on the models that aimed systematically to generate the distribution of original gas contents shown in Fig. 5, as well as the distribution of overburden values in a bivariate normal distribution. In this process, the correlation coefficient between the data pairs was matched, and the values of Q5 and Q95 were determined from the resultant distribution of population. After this step, the coefficients of the quadratic equations, which were initially arbitrary for Q5 and Q95, were iteratively determined by changing overburden depths and by targeting the Q5 and Q95 values in a goal-seek manner to minimize the standard errors of predictions. For these runs, 20,000 simulations were performed. The results of these analyses and the equations for Q5 and Q95 are also given in Table 2.

3.2. Gas-in-place (GIP) calculation

One of the key steps in forecasting gas emissions during and after mining is to calculate the volume of GIP that will potentially migrate to the underground mining environment. The simplest method for calculating the GIP for coal seams is based on commonly available geologic mapping data for the mine site and using site-specific gas content data (Diamond, 1982), as follows:

$$\mathrm{GIP}=(\rho \times \mathrm{h} \times \mathrm{A})\mathrm{GC} \quad (1)$$

where GIP is gas-in-place in coal; ρ is coal density; h is coal thickness; A is the area that coal occupies; GC is the gas content of coal (volume-to-mass ratio), in ft^3 gas/ton of coal.

A more elaborate approach is a reservoir analysis-based volumetric approach (Karacan and Diamond, 2006) given in Eq. (2). Volumetric-based calculations may also be used to determine the gas-in-place for coal beds in a specific geographic area. This approach both relates the volume of gas in the reservoir at reservoir conditions to the volume at surface conditions, treating separately the volume of free gas in fracture porosity and adsorbed gas in bulk volume.

$$\mathrm{GIP}=\mathrm{Ah}\left(\frac{43560\varphi_{\mathrm{f}}(1-\mathrm{Swf_i})}{\mathrm{Bg_i}}+1.359\,\mathrm{GC}\,(1-\mathrm{f_a}-\mathrm{f_m})\right). \quad (2)$$

In this work, a pseudo-volumetric method was used to calculate gas-in-place for coal seams. The final form of the equation, without including moisture content (f_m), which is used after geostatistical modeling is:

$$\mathrm{GIP}=\mathrm{Ah}\,\mathrm{GC}\,\rho(1-\mathrm{f_a}). \quad (3)$$

In this equation, GC is the gas content of coal (determined as explained in Section 3.1 for each coal seam). “A” is the area, “h” is thickness of a particular coal bed of interest at a specific point, f_a is the ash content of coal and ρ is its bulk density.

3.3. Ash content and density of coals

Ash in coal is a combination of all non-organic matter including clays and minerals. Ash content is strongly dependent on the primary paleo-depositional environment, the changes in the climate and various precipitations during the peat-forming process, and the present hydrogeology of the area at a particular depth. Although there is no a priori reason that ash content of coals should correlate with depth, it has been observed in West Virginia that ash content does indeed decrease on average for coals in the Monongahela Group from the Waynesburg coal to the Pittsburgh coal (West Virginia Geological and Economic Survey, 2005), similar to Fig. 6.

Ash is considered as a constituent of coal that does not have a significant methane sorption capacity. Therefore, its amount should be determined for GIP calculations (Eqs. (2) and (3)).

In addition, ash has a higher density than organic matter (112.4–137.4 lb/ft^3; 1.8–2.2 g/cm^3) and thus ash content is one of the factors that most influences coal density.

Ash contents of coal seams within a thick stratigraphic column usually follow a scattered trend, making it difficult to establish a simple correlation (Fig. 6). In addition, there are variations within each seam as a function of overburden depth, as observed from scatter of the data given in Fig. 6 and from the correlation coefficients presented in Table 2. Therefore, a probabilistic approach of uncertainty based on ash-content distributions of the individual seams over the depth they exist seems to be the best method to determine ash contents of individual coals. This method requires bivariate distribution analyses of two random functions for determining joint probabilities of occurrences of different values. In this study, these functions were assumed to be normal for distributions of depth and ash contents of individual seams.

Data for ash contents for the coals of this study were taken from Diamond et al. (1986). The data were partitioned for each seam and was analyzed using bivariate normal distributions to determine ash content at Q5, Q50, and Q95. For these analyses, a similar technique described in Section 3.1 for gas contents was performed using a combination of bivariate distribution analyses and Monte Carlo simulations. These analyses effectively treated for each seam such that at each depth ash content had a distribution function, from which probable values could be determined at Q5, Q50, and Q95 to generate functional relationships. The values of ash at Q5, Q50, and Q95, as well as their standard errors from MC simulations and the equations that represent ash values as a function of depth, are given in Tables 3 and 4.

Ash content values calculated for individual seams at different quantiles were later converted to their bulk densities using the correlation that was established for these same coals from the data given in Fig. 7. The correlation between ash content and bulk density is given in Eq. (4). Ash and density correlations were built and used in the absence of spatial data of these attributes from analyses of cores of the exploration boreholes.

$$\text{Density(g/cc)} = 0.0001\ (\text{Ash})^2 + 0.0028(\text{Ash}) + 1.3019 \quad (4)$$

3.4. Displacements of major non-coal strata during mining

As discussed in Section 2, major non-coal strata within the possible gas emission zone in the area of study are the Fishpot limestone (FPLS), Sewickley sandstone (SWSS) and Uniontown sandstone (UNSS). Properties of these rock units are important for movement of gas within the gas emission zone. If these strata subside and fracture vertically and horizontally (termed “displacement” collectively in this paper), then all sources of gas-in-place will be in communication with each other, and potentially will be in communication with the mine as well. If these strata do not displace significantly, then gas sources may be isolated from each other. Correlating maximum displacement locations of major non-coal strata with high gas-in-place locations in the gas emission zone helps in predicting those locations of high gas inflows into the mines and can best locate gas capture boreholes.

Displacements were globally described in accordance with Karacan and Goodman (2011a) using the field data presented in Mazza and Mlinar (1977) for southwestern Pennsylvania. These data, which show that strata displacements are a function of distance from the top of the mined coal seam (the Pittsburgh seam in this case) are given in Fig. 8. This figure shows that displacements are at a maximum of ~2–3 ft close to the mining zone and decrease with increasing distance from the mined seam. Eventually, fracturing and separations cease around 350 ft above the mining horizon.

Strata displacements and their probabilities were described in Karacan and Goodman (2011a). Means (μ) and standard deviations (σ) of displacements and distances from the Pittsburgh seam and the correlation coefficients (ρ) between these variable pairs that were used in calculating joint probability distributions for these variables are given in Table 5.

The bivariate normal probability calculations and representations of probabilities of observing displacements ≤4 ft with four-parameter logistic functions were used to quantify displacements. Results showed that displacements in southwestern Pennsylvania, as a result of mining of the Pittsburgh seam, could be represented by the values of the dependent variable at 50% value of the independent variable up to distances of 350 ft. The polynomial representation of these coefficients gives a Pearson's correlation coefficient of 0.9952 (Table 5). This relation was used to calculate displacements of FPLS, SWSS, and UNSS as a function of their distances from the Pittsburgh seam at exploration borehole locations, which later were used for geostatistical modeling of strata displacements in these three major rock layers.

4. Data preparation and modeling methodology

4.1. Data extraction and preparation

The data used in geostatistical modeling were obtained from 276 vertical exploration boreholes drilled over the mining area shown in Fig. 2. These boreholes and their spatial locations are shown in Fig. 9. For modeling that will be discussed in detail in the forthcoming sections, these data were assigned to a 100 × 100 Cartesian grid in which each grid was 189 ft in the x-direction and 205 ft in the y-direction. In preparing the data, the thicknesses of each identified layers of each of the coal and non-coal units were combined, so that each unit would be represented as a single layer. Accordingly, the average of the depths of these layers was taken as the representative depth of each unit, as were their depth-dependent attributes.

All empirical data from the boreholes had identified coal and non-coal formations drilled along the entire length of the boreholes. Since the top of the gas emission zone for mines operating in the Pittsburgh seam was around 350 ft above the top of the Pittsburgh coal (Karacan and Goodman, 2011a; Mazza and Mlinar, 1977), the data beyond this interval were excluded from further analyses. Thus, Fig. 9 shows only the coal and non-coal layers within the expected gas emission zone. In this figure, each data point represents an identified formation, with different colors representing their elevation using the top of the Pittsburgh seam as a reference datum.

To calculate gas-in-place in coals and in different sections of the gas emission zone, the coal beds within the 350-ft interval above the Pittsburgh seam, and including the Pittsburgh seam, were identified and isolated from the rest of the data as separate datasets. These coal beds were the Pittsburgh seam (main bench—PCMB), Pittsburgh rider seams (PCR), Redstone coal (RDC), Sewickley coal (SWC), Uniontown coal (UNC), and Waynesburg coals (both upper and lower—WBC). These data were further analyzed carefully to extract erroneous data points and to see whether they appeared as a single layer or as splits. In case of splits or multiple layers of the same seam, data were combined as noted before. Therefore, the maximum number of data points for each unit was equal to the number of boreholes when a particular seam was present in all boreholes, and the number of data points was less than the number of boreholes when the seam was missing at a particular location (Table 6).

For coal seams of interest, three attributes were determined at each spatial position for geostatistical modeling and for calculation of gas-in-place using Eq. (3). These attributes were overburden depth, thickness of coal, and gas content. Results of univariate statistical analyses of these data for each coal seam are given in Table 6.

A similar data extraction and preparation procedure was also performed for non-coal layers as well. For these layers, two attributes were determined at each spatial position for geostatistical modeling. These attributes were overburden depth and displacements, calculated using distance from the Pittsburgh seam at each borehole location. Results of univariate statistical analyses of these data for each of the non-coal layers are given in Table 7.

The frequency distributions of the data (histograms) of each of these attributes for both coal seams and non-coal layers were also checked for their Gaussian behavior. Olea (2009) and Remy et al. (2009) state that for some of the geostatistical modeling and simulation techniques to be applicable without the need of transformation of the data, the data should follow a Gaussian (normal) distribution. Plotting histograms of depth, thickness, and gas content data for coals and of depth and displacements for rock layers showed that the data were not exactly Gaussian in all cases. Therefore, automatically, all distributions in this work were transformed to normal scores by targeting a Gaussian distribution with mean 0 and variance 1. Semivariograms were then modeled on the normal-score data. However, the values of the attributes were transformed back to the original space during simulations by targeting the original distribution.

Examples of these histograms for thickness data of Waynesburg (WBC) and depth of Sewickley (SWC) coals, and normal-score transformation of these attributes are shown in Fig. 10.

4.2. Geostatistical modeling of target attributes of coal and non-coal layers

The Stanford University Geostatistical Modeling Software (SGeMS) was used for spatial correlation analyses and for stochastic (sequential Gaussian) simulations. SGeMS implements several geostatistics algorithms for modeling of earth systems and phenomena that exhibit space-time distributions (Remy et al., 2009). The software also has a graphical

user interface and a script compiler that gives the user ease and flexibility to implement complex problems. It includes several of the algorithms that are in the GSLIB—Geostatistical Software Library (Deutsch and Journel, 1998) in its platform.

4.2.1. Spatial correlation analyses using semivariograms—Semivariogram analysis, which allows for the examination of whether the data are correlated with distance, was done for all coal properties used to calculate GIP (thickness, gas content, and overburden depth) and displacement of rock layers. If a spatial correlation emerges in the dataset, directional semivariograms should start from low values and increase up to the variance of the sample data. The knowledge of spatial correlations and the ranges over which such correlations are observed, along with the knowledge of the mean of the data, are also taken into consideration when estimating the spatial distribution of parameters and their uncertainty within the Cartesian grid domain. This consideration is achieved by implementing kriging or stochastic methods such as sequential Gaussian simulations.

The semivariogram, γ (**h**), measures the average dissimilarity between two variables—for example between the values of a parameter (**x**) at location **u** and at a location **u** + **h**. Assuming stationarity, the semivariogram γ (Z(**u**), Z(**u** + **h**)) depends on a lag vector **h**: γ (**h**). Thus, the experimental semivariogram is computed by, e.g., Remy et al. (2009):

$$\gamma(\mathbf{h})=\frac{1}{2\mathrm{N}(\mathbf{h})}\sum_{\alpha=1}^{\mathrm{N}(\mathbf{h})}[z(\mathbf{u}_\alpha)-z(\mathbf{u}_\alpha+\mathbf{h})]^2. \quad (5)$$

In this description, *z* (**u**) is the value of the parameter at location **u** and N (**h**) is the number of data pairs separated by vector **h**. Semivariograms established using this approach on field or spatially distributed experimental data are generally called empirical or, more conventionally, experimental semivariograms.

Experimental semivariograms, whose data are usually scattered, are modeled with analytical functions (called analytical semivariograms), which serve three main purposes. Above all, they ensure unique solutions. Secondly, they allow for the computation of a semivariogram value, $\gamma(\mathbf{h})$, for any given lag vector, **h**. Finally, they allow for filtering of the noise, which is usually a result of either imperfect measurements or lack of data, from experimental semivariograms. The general semivariogram model is

$$\gamma(\mathbf{h})=c_0\gamma^{(0)}(\mathbf{h})+\sum_{\mathrm{p}=1}^{\mathrm{P}}c_\mathrm{p}\gamma^{(\mathrm{p})}(\mathbf{h}). \quad (6)$$

In this general model, the first part of the equation is “nugget” effect, with $c_0 \geq 0$. “P” is the number of nested structures (the second part of the equation), each of which is defined by specific analytical models with a variance contribution, $c_p \geq 0$. Thus, a linear combination of analytical semivariograms can be used to describe possible nested structures in an experimental semivariogram. The most common analytical semivariograms that can either

be used by themselves or as nested structures to describe more complicated experimental semivariograms are

1. Spherical model with range “a”:

$$\gamma(\mathbf{h})=\begin{cases}\frac{3}{2}\frac{\|\mathbf{h}\|}{\mathrm{a}}-\frac{1}{2}\left(\frac{\|\mathbf{h}\|}{\mathrm{a}}\right)^3 & \text{if}\|\mathbf{h}\| \leq \mathrm{a}\\ \gamma(\mathbf{h})=1 \quad \text{otherwise}\end{cases} \quad (7)$$

2. Exponential model with practical range “a”:

$$\gamma(\mathbf{h})=1-\exp\left(\frac{-3\|\mathbf{h}\|}{\mathrm{a}}\right) \quad (8)$$

3. Gaussian model with practical range “a”:

$$\gamma(\mathbf{h})=1-\exp\left(\frac{-3\|\mathbf{h}\|^2}{\mathrm{a}^2}\right). \quad (9)$$

The upper bound of an analytical model is called the “sill.” The range is the lowest lag at which the semivariogram reaches the sill. The sill is reached asymptotically in the case of exponential and Gaussian models. The distance at which 95% of the sill is reached is called the “practical range.”

Data in the earth sciences often display some degree of anisotropy both areally and with depth. Therefore, it is always beneficial to assess the possible effect of anisotropy on semivariograms in multiple directions. In this study, semivariogram modeling was performed on the normal-score distribution of each of the attributes, as offered earlier, and based on the approach described in Olea (2006). Directional experimental semivariograms of normal scores were searched in each case with 0°, 45°, 90°, and 135° starting from the north and changing toward the east direction of lag vectors. In addition, an omni-directional semivariogram was modeled in each case.

Attention was given to find a model that would best fit each of the above semivariograms. Lag separation distances, the number of lags, and lag tolerance were different in each case, depending on the nature of data and the spatial correlations they showed. The lag separation distances were generally between 150 and 500 ft, with 75–250-ft lag tolerances, as described in Olea (2006). In accordance with the selection of lag distances, usually 30–50 lags were enough to define the ranges. A tolerance of azimuth was defined as 22.5° in each case, and bandwidths of approximately 2500 ft were used.

Modeling of semivariograms showed that there was not a significant anisotropy arising from the spatial locations, directions, and the magnitudes of the attributes. Therefore, the isotropic modeling approach was adopted in defining the plane rotation angles of search ellipsoid and in simulations. Due to isotropy, the rotation angles of the search ellipsoid, i.e. azimuth, dip, and rake, were taken as 0, whereas the three radii of the ellipsoid were taken as the ranges of the semivariogram in all cases.

Example experimental semivariograms for the normal-score data of WBC thickness and SWC depth and the analytical functions representing those are shown in Fig. 11A and B, respectively. The analytical semivariogram models of the variables for the six coal seams (PCMB, PCR, RDC, SWC, UNC and WBC) and three non-coal layers (FPLS, SWSS, UNSS) are summarized in Tables 8 and 9, respectively. Please note that the types of the models, their nugget parameters, and sills, as well as geometric ranges, depend on the geological unit and the attributes.

4.2.2. Sequential Gaussian simulations and analyses of data—Sequential Gaussian simulation (SGSIM) is a semivariogram-based simulation technique and a special case that takes advantage of convenient properties of Gaussian random functions (e.g. Gómez-Hernández and Cassiraga, 1994; Remy et al., 2009). Simulated results, or so-called realizations, render spatial patterns consistent with the input data and semivariograms. Realizations can be seen as numerical models of possible distribution of the simulated property in space. In this work, 100 realizations for each attribute of interest were generated by using a different seed number for every attribute to ensure the randomness. This set of simulations was used for analyses of uncertainty and distribution of properties in the study area.

Simulation is superior compared to kriging particularly in assessing uncertainty. Although both SGSIM and simple kriging (SK) were performed in this study, SGSIM results will be discussed in more detail in forthcoming sections. In practice, the realizations take the form of a finite number of simulated maps, with equal probability to represent the unknown true map. Therefore, each grid in each of these realizations, or simulated maps, generates a distribution of the particular attribute. These distributions can be used to analyze the data statistically for variances and to evaluate the uncertainty associated with various values in a probabilistic sense. Furthermore, since the “L” number of simulated realizations of a property “$z^l(\mathbf{u})$” all have equal probability, the cell-by-cell averaging of these realizations provides a single estimated value with a least squares error according to

$$z_E^*(\mathbf{u}) = \frac{1}{L}\sum_{l=1}^{L} z^l(\mathbf{u}) \quad (10)$$

where $z_E^*(\mathbf{u})$ is called the E-type estimated value, or conditional expectation (e.g. Deutsch and Journel, 1998), resulting in a map with local accuracy similar to that of a kriging map, which provides only an estimation mean and the variance. In a similar way, all values at the same cell for all L realizations can be used to calculate the cell mean. It is also possible to calculate the cell variance and prepare a map with the values resulting for all cells in the grid.

Fig. 12 shows the cell variance for SGSIM (A) and the SK variance (B) resulting from modeling the depth of the Pittsburgh seam. It should be noted that the SGSIM variance is more irregular than the SK variance. More importantly, experiments conducted using censored exhaustive samples have demonstrated that confidence intervals associated with kriging may be biased—too narrow for high values, and too wide for low values—especially

for skewed distributions. Thus, the use of stochastic simulation is a better option if proper modeling of confident intervals and quantiles is an important objective of a study.

In this study, for an initial assessment, E-type maps of simulated attributes were compared with maps of simple kriging (SK) in relation to some general properties that describe the distribution of random functions generated by these two techniques. However, for detailed analyses and for evaluating and discussing the results, SGSIM simulations were preferred over kriging due to reasons mentioned above and will be discussed for the rest of this paper.

5. Results and discussion

5.1. Elementary data analyses on results of simulations

All modeling studies and their results require some level of verification. In this study, the results of sequential Gaussian simulations of modeled attributes were compared with the original data before proceeding with calculations of GIP and the associated uncertainties. These comparisons required development of histograms and Q–Q plots of hard data, along with SGSIM realizations and calculation of elementary descriptive analyses. The analysis procedure is schematically shown in Fig. 13 for thickness of the Pittsburgh seam and was applied to each of the simulated parameters for evaluations of results.

Basic statistical analyses of the data obtained from E-maps of simulated attributes of coals and non-coal units, with the hard data given in Tables 6 and 7, showed that almost all of the basic statistical parameters are similar. This indicates that average results from simulations have similar properties in relation to the ranges and limits of the hard data. However, it should be recognized that the variances obtained from E-data are less because the point-wise averages of simulated data in E-maps have less dispersion compared to both hard data and to individual realizations. For instance, Fig. 14 shows example histograms of Waynesburg coal thickness and Sewickley coal depth plotted from the 50th realization and from the E-type maps (point-wise average of 100 realizations). Histograms of the hard data for the same properties and formations are given in Fig. 10. Comparison of distributions from the presented realizations and E-type maps with the hard data shows that the histograms of individual realizations are very similar to the hard data, since they are generated to closely match the cumulative probability distribution of the original data. On the other hand, E-type data have less dispersion due to averaging of results from a large number of realizations compared to the original data and to individual realizations, as expected. This was the case for all modeled attributes. Therefore, individual realizations and properties derived from those attributes were used to calculate gas-in-place and uncertainties.

In addition to comparisons of basic statistical parameters outlined above, Q–Q plots were prepared for each modeled attribute for their hard data versus E-type data quantiles and for hard data versus individual realizations. Q–Q plots are used to compare probability distributions. A straight line is an indication of equality between the distributions being compared and that the data in both axes have similar quantile values (Krishnamoorthy, 2006).

The Q–Q plot analyses conducted in this work gave acceptable linear trends between hard data and realizations, as well as between E-type maps. Fig. 15 shows, as an example, this comparison for thickness of the Waynesburg coal. This figure shows that comparisons of both types of SGSIM data give nearly linear relations with the hard data from which they are generated, and thus the probability distributions of all data are almost the same. Note the smoothing in the E-type map, revealed by higher modeled values when the empirical values are low, and lower modeled values when the empirical values are high. An E-type map shares a similar smoothing effect as a kriging map.

5.2. Gas-in-place and displacement results in the emission zone and their uncertainties

Since spatial features and uncertainty play an important role in predictions of GIP and methane emissions that result from the gas emission zone, individual realizations, rather than E-type maps, of modeled attributes from SGSIM were used to create realizations of GIP for further analyses and computations.

GIP and displacement calculations for the gas emission zone and the uncertainty evaluation strategy were as described below.

1. GIP in various sections of the gas emission zone that are important for longwall mines were calculated for:
    - The Pittsburgh seam (PCMB)—mined coal whose emissions during mining directly enter the ventilation system. This emission is usually controlled by effective design of the ventilation system.
    - Caved zone—combination of gas-in-place of lower seams in close proximity to the mined coal bed. These seams are the Pittsburgh rider (PCR) and Redstone coal (RDC). The emissions from this zone potentially enter the ventilation system directly after caving or continue to release within the gob. The hazard of these emissions is that they may build up in the gob and may enter the mine environment with leakages due to fluctuations of atmospheric pressure.
    - Fractured zone—methane emissions that result from the coal beds and other gas sources that are within the fractured area of gas emission zone. These sources are usually sufficiently above the mined coal bed so that they are only fractured, not caved. The methane from these sources may combine through the fractures within interlayer non-coal rock units and may act as a single source from a GIP point of view. The emissions from these formations are usually captured with gob gas ventholes. If these boreholes do not operate effectively, methane within the fracture zone may migrate into the caved zone and eventually into the working areas. In the study area, the Sewickley coal, Uniontown coal, and Waynesburg coal are considered to be the main sources of methane in the fractured zone.

In addition to assessing these three distinct zones of deformation for the entire model area, GIP in the following longwall panel series was also calculated for N–F panels, and G–K

panels. The reason why these two panel series were evaluated separately is that the methane from the ventilation system was controlled with two separate bleeder fans (Figs. 2 and 3).

The values of GIP for individual coals and longwall gob zones, as well as displacements from realizations, were calculated at 5%, 50%, and 95% quantiles (Q5, Q50, Q95). These quantiles represent the values where each estimated value is ranked at 5%, 50%, and 95% in the distribution of results, and the probability of the estimated values is lower than the actual unknown values. Therefore, the data of any attribute at 5% quantile are the estimated values at 5% probability, and can be considered as the lower limit. Similarly, Q95 is the data with 95% chance of being higher than the actual value and is considered as the upper limit. Between these, Q50 has a special meaning, representing the median of the possible population distribution. Q50 is called M-type where each estimated value has a 50% chance to be higher than the actual value.

5.2.1. Gas-in-place assessment—Eq. (3) and the ancillary correlations given in Eq. (4) and in Tables 1–4 were used for calculation of GIP. The terms of Eq. (3) were obtained from simulations over the simulation area “A” as realizations having 100×100 grids. Therefore, 100 realizations of GIP, each of which had 10,000 values, were generated by using 100 different realizations of each of the terms that were simulated or built using the correlations.

It is important to document GIP of various coals that are within the gas emission zone from gas emissions in longwall-mines and from an uncertainty quantification point of view. Therefore, before cumulative GIP values for different zones of longwall gobs and their uncertainties are presented, GIP values calculated for each of the coal seams are given in Fig. 16, which presents the 50th GIP realization for PCMB, PCR, RDC, SWC, UNC and WBC.

The realizations given in Fig. 16 show that each coal seam has different GIP within the 8900-acre area shown in Fig. 2. The distributions of the amount of gas per acre of these seams, which are computed from each realization using 10,000 data points, are given in Fig. 17. These plots are in terms of relative and cumulative relative frequencies of per-acre GIPs. As these data show, PCMB, SWC, and WBC have the highest methane amounts per acre, respectively. Within the gas emission zone, these seams are followed by PCR. Although PCR has high ash content and consists of relatively thin seams, the combined thickness of these seams and their contributions can be a significant methane source in longwall gob. Among these six coal seams, RDC and UNC have the least amount of gas per acre due to their thickness and discontinuous nature. Basic statistical measures calculated from each of these distributions are given in Table 10.

Although the distributions given in Fig. 17 and the values of Table 10 can be helpful to obtain a general idea about the gas-in-place in these seams, they are based on only one realization (50th realization) randomly selected from 100 different possible solutions for the model area. Therefore, a quantile analysis was performed using all 100 GIP realizations to find the realizations that represent Q5, Q50, and Q95 of the entire distribution. In other words, to assess uncertainty, the realizations and their associated GIP data below which the unknown real value will be less were defined, with 5%, 50%, and 95% probabilities.

In order to determine GIP with Q5, Q50, and Q95 for each seam, cumulative GIPs in the model area were determined by summing the GIP of 10,000 cells in each of the 100 realizations. Next, cumulative GIP values calculated for each realization were ranked to determine the GIP values and corresponding realizations that give 5%, 50%, and 95% of the distribution. Table 11 shows the Q5, Q50, and Q95 for cumulative GIP, the average GIP per acre, and the corresponding realizations for all coal seams.

Table 11 shows that UNC and RDC coals have the least amount of gas per unit of area, whereas PCMB, SWC, and WBC coals have the highest amount of in-place methane. These amounts relate to the higher thicknesses of these seams and their relatively less ash contents. According to estimations, GIP of per acre of PCMB can be ~1.57 MMscf at Q5 and ~1.59 MMscf at Q95. Therefore, the uncertainty within this quantile interval is 0.02 MMscf per acre in the Pittsburgh seam. The PCR seams, on the other hand, are generally thin and have high ash contents. However, when there are multiple thin rider seams, their in-place gas content may be approximately 0.48 MMscf/acre at Q5 and 0.50 MMscf/acre at Q95. Therefore, multiple thin rider seams can be a significant gas resource for the caved zone.

SWC and WBC coals are important seams in the fractured zone of longwall mines. According to quantile estimations presented in Table 11, SWC and WBC can have as much as 10.3 and 6.2 Bcf of cumulative methane with Q50, respectively, in this model area. These cumulative gas-in-place amounts translate to 1.16 MMscf and 0.69 MMscf averages for in-place methane per acre of these seams, respectively, at Q50.

GIP realizations of the caved zone and fractured zone can be produced and quantile estimations can be made once GIP realizations of individual seams over the entire model area are generated, For this purpose, individual GIP realizations of PCR and RDC for the caved zone, and realizations of SWC, UNC, and WBC for the fractured zone, were summed grid by grid. Thus, 100 GIP realizations were generated for both the caved zone and fractured zone. After this step, a procedure similar to that described for individual coal seams was conducted to find cumulative GIP in each realization and for ranking and quantiles estimation.

Fig. 18 shows the relative frequency and cumulative relative frequency distributions of GIP amounts of 100 realizations computed for the caved zone (Fig. 18A and B) and fractured zone (Fig. 18C and D). These distributions were used in ranking and to determine the amounts of GIP and corresponding individual zone realizations at Q5, Q50, and Q95, which are given in Table 12.

Table 12 shows that both the caved zone and fractured zone can contain a significant amount of gas. The caved zone for the modeled area can have as much as 5.1 Bcf of methane at Q5 and 5.35 Bcf at Q95. The difference of cumulative GIP in this quantile range is 250 MMscf, which can be a significant amount of gas for ventilation purposes. The median GIP for the caved zone is 5.21 Bcf. The fractured zone, on the other hand, can have much higher amounts of GIP in this area due to the existence of gassier and thicker coal seams with less ash content. The cumulative GIP amounts in this zone are 16.8 Bcf and 17.2 Bcf for Q5 and Q95, respectively, with a median value of 17.0 Bcf. In light of the individual coal seam data

discussed above, the number of layers (thickness) of the PCR has potential to affect the gas-in-place in the caved zone, whereas the gas-in-place for SWC and WBC should be taken into account for the fractured zone.

Fig. 19 shows the distributions of potential GIP in various important zones of the gas emission interval per acre of mining in order to summarize gas-in-place evaluation of the model area. These distributions represent Q5, Q50, and Q95 from their corresponding realizations. This figure shows that the GIP per acre of mining in the Pittsburgh seam can vary between 0.25 MMscf and ~1 MMscf in the caved zone, ~1.2 and ~2.1 MMscf in PCMB, and 1.25 MMscf and 2.75 MMscf in the fractured zone. Basic statistics of these distributions at various quantiles are given in Table 13.

Overall, mines operating in the Pittsburgh seam in this 8900 acre area or in a similar size area will have total GIP (PCMB + caved zone + fractured zone) between 35.9 Bcf and 36.6 Bcf, with 5–95% probability. These GIP quantities will amount to be 4.0 MMscf and 4.2 MMscf per acre on average for 5% and 95% quantiles, respectively. Therefore, a degasification system using gob gas ventholes and the mine's ventilation system should be designed to collectively handle this amount of methane originating from mining 1 acre of PCMB. In summary, methane capture and ventilation system design should be based on the gas-in-place amounts (for mining per acre of PCMB) given in Tables 12 and 13.

5.2.2. Application of gas-in-place assessments for the panel series within study area—The cumulative GIP results and GIP per acre estimations discussed in the previous section are based on the entire 8900-acre model area (Fig. 2) and on potential emissions if one decides to design a Pittsburgh seam mine.

This section investigates the GIP amounts in typical panel series, such as the ones that were mined in the model area. These panels are shown in Fig. 2. Two bleeder fans were used as part of the main ventilation system to remove in-mine emissions from panels N–K. Bleeder fan 2 (BF-2) was mainly used to remove methane emissions from panels N–F during their extraction, while bleeder fan 3 (BF-3) ventilated panels G–K as they were being mined. In addition, gob gas ventholes were drilled in an effort to capture methane from the fractured zone. Methane production rates of these fan and gob gas venthole systems are given in Fig. 3.

GIP calculations in different sections of the gas emission zone were also conducted for these two main panel areas because general ventilation in these panels was established via two main fans and because these two areas can represent typical mining series in the PCMB. For this purpose, panel grids N–F and G–K within the model area were blanked for the PCMB, the caved zone, and the fractured zone with numerical techniques as shown in Fig. 20. This was done to calculate both areas and volumes with integration using the trapezoid rule in these panel regions.

The planar areas for N–F panel and G–K panel series were calculated as 1290 acres and 1740 acres, respectively. These size panel series can be considered as typical of longwall mines operating in the Pittsburgh seam. N–F and G–K panel series totals to 3030 acres,

which is about 35% of the entire model area. The cumulative gas-in-place amounts within PCMB, the caved zone, and the fractured zone of these separate panel areas were calculated using realizations corresponding to the Q50 quantile, as an example, and are shown in Table 14. This table shows that GIP in the N–F series was lower than that in the G–K series in all sections of the gas emission zone, mainly due to the differences in mined areas and the location of panels in relation to high-gas regions (Fig. 20) of the model area. This table shows that cumulative GIP in PCMB was less than ~1.8 Bcf with 50% probability in the N–F series, and less than 2.5 Bcf in the G–K series. The data in Table 14 further show that GIP estimates for the caved zone in these two panel series varied between less than 0.7 Bcf and 0.8 Bcf in the N–F and G–K, respectively, with 50% probability. On the other hand, the highest gas potentials were estimated for the fractured zone where cumulative GIP ranged from 2.3 Bcf (for N–F) to 3.1 Bcf (for G–K) at Q50. These GIP values can be considered as methane amounts to be released with 50% probability for the Pittsburgh seam longwall series, and they can be used for estimating cumulative methane emissions and for properly designing methane capture and ventilation systems.

Distribution of GIP potential (Q50) per acre of mining in these panel districts are shown in Fig. 21. These distributions show that per-acre estimations for Q50 are very close to the ones shown in Fig. 19 for the entire model area. This is due to the absence of major local heterogeneities in the model area that would affect the GIP estimations. Basic statistical measures of these distributions are given in Table 15. In general, mines operating in the Pittsburgh seam may either consider the gas amounts as per-acre of mining values given in Tables 13 and 15, or may consider the total gas-in-place volumes given in Table 14 for these two panel districts. However, it should be noted that the GIP estimates presented in Tables 14 and 15 are given only for the 50% quantile.

5.2.3. Non-coal strata displacement considerations for emission zone modeling—This last section briefly addresses the displacements of non-coal formations within the gas emission zone of longwall mines. Displacements in rock strata, either vertical or horizontal, and their magnitudes are particularly important when these formations are interbedded between various gas sources (coal seams, free gas pockets, gobs of abandoned mines, active mines, etc.), in that they create migration paths between these sources and active mines. Therefore, it is generally recommended to evaluate gas-in-place in combination with spatial distribution of rock displacements in various horizons within the gas emission zone.

Within the stratigraphy of the modeled area, the Fishpot limestone, Sewickley sandstone, and Uniontown sandstone were identified as important non-coal strata whose displacements at various locations might influence in-mine emissions and the efficiency of gas capture. Therefore, displacements of these formations were modeled as explained in previous sections.

Displacement amounts were estimated using a similar approach described for gas-in-place assessment, i.e. by ranking simulation results of displacements in three non-coal strata to find the quantiles and their corresponding realizations. Fig. 22 shows distributions of displacements of these three major non-coal formations over the entire model areas for Q5,

Q50, and Q95. This figure shows that the displacements calculated, using 10,000 data points in each realization at various quartiles, are close to each other. Therefore, quartile values may not be as critical as the distribution of the displacement values themselves and their locations over the panels. In this regard, FPLS had the largest displacement of all, followed by SWSS and UNSS. Average estimated displacements in these formations were about 1.8 ft, 1.4 ft, and 0.9 ft, for FPLS, SWSS, and UNSS, respectively. Basic statistical values of the distributions shown in Fig. 22 are given in Table 16.

Although the information about displacements of rock strata within the gas emission zone may be helpful, it is difficult to correlate these with in-mine emissions and methane capture designs from fractured strata. Higher GIP at a particular spatial location is more likely to move directly toward the mining environment if the rock strata directly below it displace more when compared to other locations. Therefore, spatial information of absolute displacements is more important than average displacements above mining panels.

Fig. 23 shows the maps of estimated displacements for FPLS, SWSS, and UNSS with Q50 quantiles. The locations of the N–F and G–K panel series are shown behind these maps as well, so that various displacements can be compared to their positions in the panels.

The maps in Fig. 23 show that the FPLS was the rock unit that experienced most displacement due to its close proximity to the Pittsburgh seam. Displacements of this unit were on the order of 2 ft or larger toward the east and south of the site. SWSS, on the other hand, experienced most of the displacement (~1.6 ft) above the N–F panels and at the east margin and middle of the G–K panel series. This rock unit is estimated to displace at a lesser degree in a channel-like region above the N–K and G–K panel series, where displacements are as small as 1 ft. UNSS had more displacement within the gas emission zone above the N–F panel series compared to the G–K series, suggesting that there may be more communication with UNC and WBC due to their proximity, and thus more emissions into the mines as the BF-2 data show in Fig. 3.

6. Summary and conclusions

Successful control of methane gas in the underground coal mine environment requires knowledge of the gas emission zone, including its size and the GIP quantity, and the displacement of the overlying strata. This work used data from 276 exploration boreholes in the Northern Appalachia Basin to identify those coal and non-coal layers deemed important for gas emissions into active and inactive longwall mining panels. The coal layers included the Pittsburgh Main and Rider coals, the Redstone coal, the Sewickley coal and its splits, the Uniontown coal, the Waynesburg coal, and the Waynesburg A and B seams—all comprising the Monongahela formation. Non-coal layers included the Fishpot limestone, the Sewickley sandstone, and the Uniontown sandstone.

Semivariograms in different directions were constructed on the normal-score data of each attribute for exploring spatial correlation of thicknesses, depth, and gas contents of coal layers. Similar semivariograms were developed for displacements of the non-coal strata. Sequential Gaussian simulations were then performed to obtain spatial distribution thickness, gas content, and displacement in the study area. Gas contents were further used,

along with the values for coal density and ash content, to estimate GIP for the various coal layers and important emission zones of longwall mines.

GIP and displacement estimates were made at the 5%, 50%, and 95% quantiles in the gas emission zone for the Pittsburgh coal (main bench), the caved zone, and the fractured zone above the two longwall panel groups. For the entire 8900 acre study area, the 50% values for GIP in the PCMB, the caved zone, and the fractured zone are approximately 14 Bcf, 5 Bcf, and 17 Bcf, respectively. The mine ventilation system and any additional degasification system (if used) should be designed to handle these gas quantities.

Longwall panels N to F and G to K totaled 1290 and 1740 acres, respectively. Estimated total GIPs at the 50% quantile were 4.8 and 6.4 Bcf, respectively. The N to F panels had lower GIP due to the differences in the mined area and the location of the panels in the lower gas region of the study area. This study showed that the GIP available for emissions for each acre of mined coal in typical longwalls varies between 0.2 MMscf and 2.5 MMscf depending on the part of the gas emission zone.

A final analysis showed that displacements of non-coal strata were similar in magnitude for the same strata between panel groups N–F and G–K. However, displacements were greatly closer to the coal seam. Calculated displacements were 1.9 ft, 1.4 ft, and 0.9 ft for the Fishpot limestone, Sewickley sandstone, and Uniontown sandstone, respectively.

Finally, geostatistical modeling and simulation methods are useful in quantitatively evaluating GIP amounts within the emission zones of longwall mines. Although, there still may be site specific considerations, limitations and uncertainties related to gas emissions, spatial distributions of various attributes, including geological heterogeneities, can be assessed using these methods to estimate the gas emissions and their potential flow paths into the working environment. Geostatistical methods and their estimates can be used to improve ventilation design and thus to improve worker safety by considering spatial distributions of gas emissions and their uncertainty applied to ventilation and degasification design. In this regard, sequential Gaussian simulation is more suited for these applications compared to kriging, since the resulting data can be evaluated probabilistically, beyond a mean and variance, to assess uncertainty.

Acknowledgments

We thank Dr. Michael Hohn of WV Geological and Economic Survey and Dr. James Luppens of USGS for reviewing and making useful comments on the initial version of this paper.

List of abbreviations and units

A	Area
Bcf	Billion cubic feet
FPLS	Fishpot limestone
GC	Gas content

GGV	Gob gas venthole
GIP	Gas in place
MMscf	Million specific cubic feet
Mscfd	Thousand specific cubic feet per day
PCMB	Pittsburgh main bench seam
PCR	Pittsburgh coal rider
RDC	Redstone coal
Real. Seq. #	Realization sequential number
scf	Specific cubic feet
SGSIM	Sequential Gaussian simulation
SK	Simple kriging
SWC	Sewickley coal
SWSS	Sewickley sandstone
UNC	Uniontown coal
UNSS	Uniontown sandstone
WBC	Waynesburg coal
$\mathbf{B_{gi}}$	Gas formation volume factor
ρ	Correlation coefficient (in Tables 1, 3 and 5)
μ	Mean
σ	Standard deviation
$\mathbf{Ø_f}$	Fracture porosity
$\mathbf{S_{wfi}}$	Water saturation in fracture porosity

References

Carroll ZL, Oliver MA. Exploring the spatial relations between soil physical properties and apparent electrical conductivity. Geoderma. 2005; 128:354–374.

Delbari M, Afrasiab P, Loiskandl W. Using sequential Gaussian simulation to assess the field-scale spatial uncertainty of soil water content. Catena. 2009; 79:163–169.

Deutsch, CV.; Journel, AG. GSLIB Geostatistical Software Library and User's Guide. 2. Oxford University Press; New York, NY: 1998. p. 369

Diamond, WP. U.S. Department of the Interior, U.S. Bureau of Mines, Information Circular No: 8898. 1982. Site-specific and regional geologic considerations for coalbed gas drainage.

Diamond WP, Schatzel JS. Measuring the gas content of coal: a review. International Journal of Coal Geology. 1998; 35:311–331.

Diamond, WP.; LaScola, JC.; Hyman, DM. U.S. Department of the Interior, U.S. Bureau of Mines, Information Circular No: 9067. 1986. Results of direct-method determination of the gas content of U.S. coalbeds; p. 95

Falivene O, Cabrera L, Sáez A. Optimum and robust 3D facies interpolation strategies in a heterogeneous coal zone (Tertiary Pontes basin, NW Spain). International Journal of Coal Geology. 2007; 71:185–208.

Gómez-Hernández, JJ.; Cassiraga, EF. Theory and practice of sequential simulation. In: Armstrong, M.; Dowd, PA., editors. Geostatistical Simulation. Kluwer Academic Publishers; Dordrecht: 1994. p. 111-124.

Heriawan MN, Koike L. Identifying spatial heterogeneity of coal resource quality in a multilayer coal deposit by multivariate geostatistics. International Journal of Coal Geology. 2008; 73:307–330.

Hindistan MA, Tercan AE, Unver B. Geostatistical coal quality control in longwall mining. International Journal of Coal Geology. 2010; 81:139–150.

Hohn ME, Neal DW. Geostatistical analysis of gas potential in Devonian shales of West Virginia. Computers and Geosciences. 1986; 12:611–617.

Karacan CÖ. Forecasting gob gas venthole production performances using intelligent computing methods for optimum methane control in longwall coal mines. International Journal of Coal Geology. 2009a; 79:131–144.

Karacan CÖ. Reservoir rock properties of coal measure strata of Lower Monongahela Group, Greene County (Southwestern Pennsylvania), from methane control and production perspectives. International Journal of Coal Geology. 2009b; 78:47–64.

Karacan CÖ. Reconciling longwall gob gas reservoirs and venthole production performances using multiple rate drawdown well test analysis. International Journal of Coal Geology. 2009c; 80:181–195.

Karacan, CÖ.; Diamond, WP. Forecasting gas emissions for coal mine safety applications. In: Kissell, F., editor. Handbook for Methane Control in Mining. NIOSH; Pittsburgh, PA: 2006. Information Circular No: 9486

Karacan CÖ, Goodman GVR. Probabilistic modeling using bivariate normal distributions for identification of flow and displacement intervals in longwall overburden. International Journal of Rock Mechanics and Mining Sciences. 2011a; 48:27–41.

Karacan CÖ, Goodman GVR. Monte Carlo simulation and well testing applied in evaluating reservoir properties in a deforming longwall overburden. Transport in Porous Media. 2011b; 86:415–434.

Karacan CÖ, Luxbacher KD. Stochastic modeling of gob gas venthole production performances in active and completed longwall coal mines. International Journal of Coal Geology. 2010; 84:125–140.

Karacan CÖ, Esterhuizen GS, Schatzel S, Diamond WP. Reservoir-simulation based modeling for characterizing longwall methane emissions and gob gas venthole production. International Journal of Coal Geology. 2007; 71:225–245.

Karacan CÖ, Ruiz FA, Cotè M, Phipps S. Coal mine methane: a review of capture and utilization practices with benefits to mining safety and to greenhouse gas reduction. International Journal of Coal Geology. 2011; 86:121–156.

Krishnamoorthy, K. Handbook of Statistical Distributions with Applications. Chapman and Hall/CRC Press; Boca Raton, Florida: 2006. p. 346

Leuangthong, O.; Khan, KD.; Deutsch, CV. Solved Problems in Geostatistics. Wiley; Hoboken, New Jersey: 2008. p. 207

Markowski A. Coalbed methane resource potential and current prospect in Pennsylvania. International Journal of Coal Geology. 1998; 38:137–159.

Mazza, RL.; Mlinar, MP. U.S. Department of Interior, U.S. Bureau of Mines Research Report No. 1607-1-77. 1977. Reducing methane in coal mine gob areas with vertical boreholes.

McFall, KS.; Wicks, DE.; Kuuskra, VA. GRI Topical Report, 86-0272. 1986. A geologic assessment of natural gas from coal seams in the Warrior Basin of Alabama; p. 80

Noack K. Control of gas emissions in underground coal mines. International Journal of Coal Geology. 1998; 35:57–82.

Olea RA. A six-step practical approach to semivariogram modeling. Stochastic Environmental Research and Risk Assessment. 2006; 20:307–318.

Olea, RA. U.S. Department of the Interior. U.S. Geological Survey, Open-File Report 2009-1103. 2009. A Practical Primer on Geostatistics; p. 346

Olea RA, Luppens JA, Tewalt SJ. Methodology for quantifying uncertainty in coal assessments with an application to a Texas lignite deposit. International Journal of Coal Geology. 2011; 85(1):78–90.

Remy, N.; Boucher, A.; Wu, J. Applied Geostatistics with SGeMS, A User's Guide. Cambridge University Press; Cambridge, United Kingdom: 2009. p. 264

Thakur, PC. Coal seam degasification. In: Kissell, F., editor. Handbook for Methane Control in Mining. NIOSH; Pittsburgh, PA: 2006. Information Circular No: 9486

Ulery, JP.; Hyman, DM. The modified-direct-method of gas content determination: applications and results. Proceedings of the International Coalbed Methane Symposium; Tuscaloosa, AL. 1991. p. 489-500.

Wackernagel, H. Multivariate Geostatistics—An Introduction with Applications. 3. Springer; Berlin, Germany: 2010. p. 387

Watson WD, Ruppert LF, Bragg LJ, Tewalt SJ. A geostatistical approach to predicting sulfur content in the Pittsburgh coal bed. International Journal of Coal Geology. 2001; 48:1–22.

Webster, R.; Oliver, MA. Geostatistics for Environmental Scientists. 2. Wiley; West Sussex, England: 2009. p. 330

West Virginia Geological and Economic Survey. 2005. http://www.wvgs.wvnet.edu/www/datastat/te/index.htm2005

Whittles DN, Lowndes IS, Kingmana SW, Yates C, Jobling S. Influence of geotechnical factors on gas flow experienced in a UK longwall coal mine panel. International Journal of Rock Mechanics & Mining Sciences. 2006; 43:369–387.

Whittles DN, Lowndes IS, Kingman SW, Yates C, Jobling S. The stability of methane capture boreholes around a long wall coal panel. International Journal of Coal Geology. 2007; 71:313–328.

Zhang C, Selinus O. Spatial analyses of copper, lead and zinc contents in sediments of the Yangtze River basin. The Science of the Total Environment. 1997; 204:251–262.

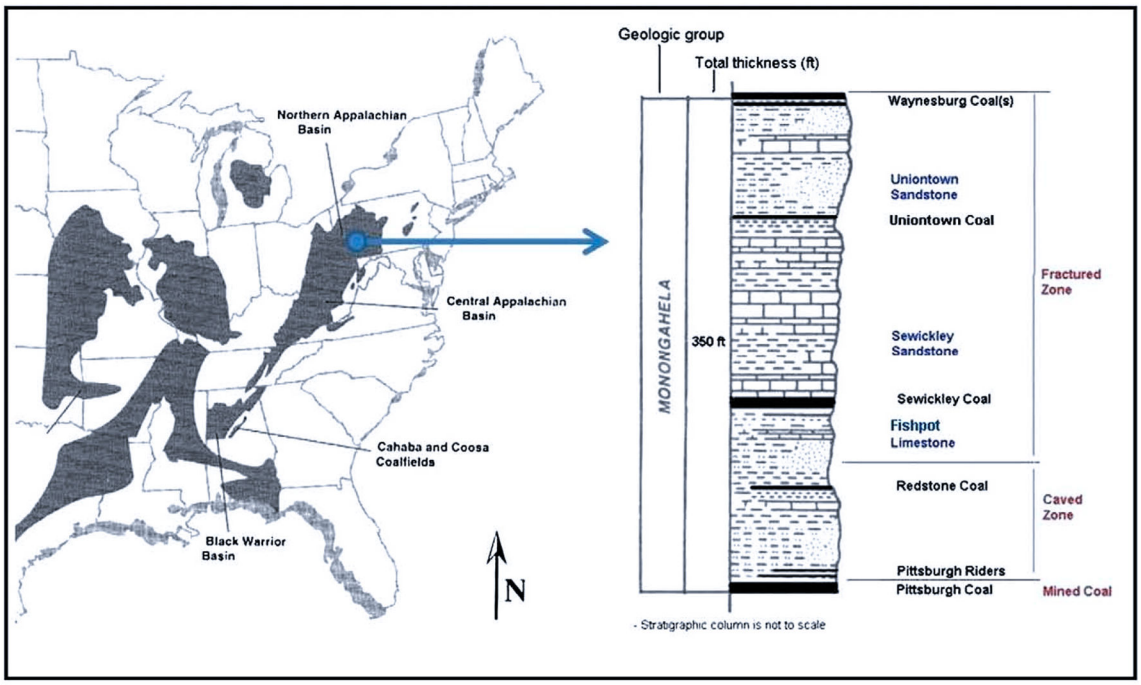

Fig. 1.

Northern Appalachian Basin and a general stratigraphic column of the Monongahela Group above the mining district studied in this paper, including various coal and non-coal layers that were modeled for gas emission zone evaluation. Different estimated sections of gas emission zone are also shown.

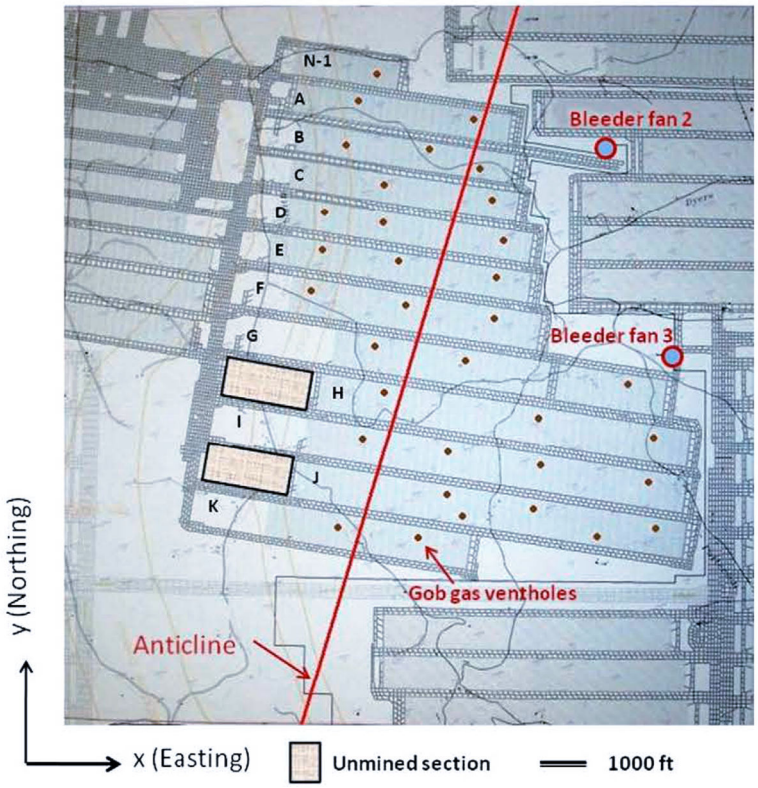

Fig. 2.
Mining district selected for this study and layout of the mined longwall panels.

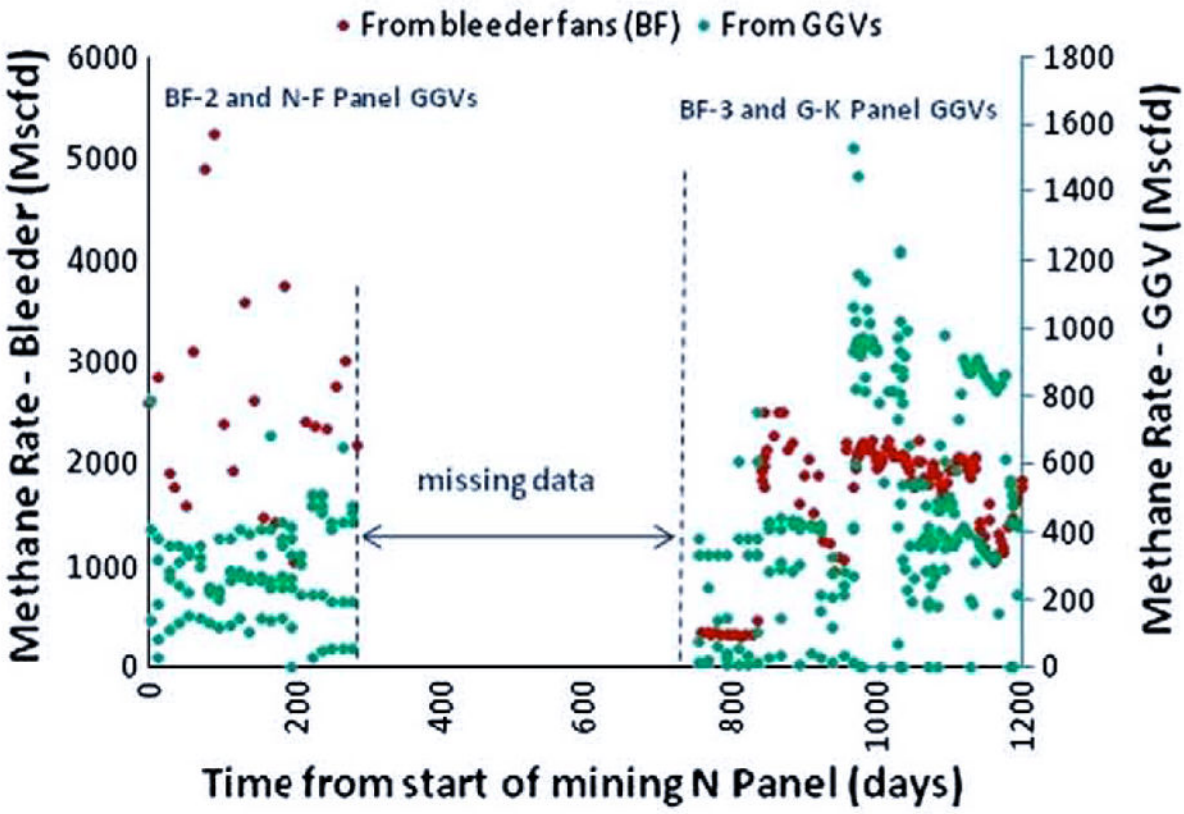

Fig. 3.

Methane production rate from longwall bleeders (BF-2 and BF-3) from gob gas ventholes drilled over panels.

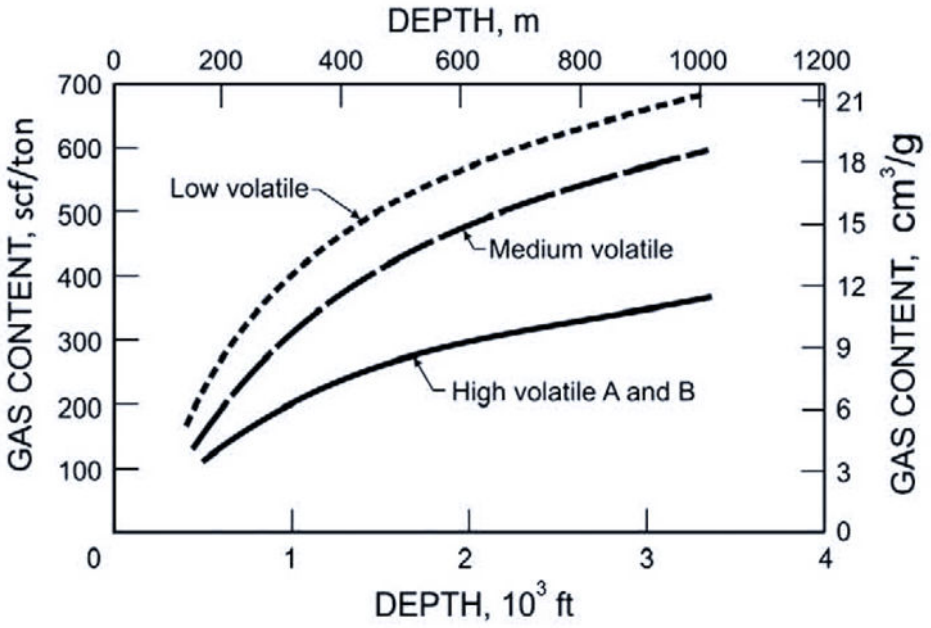

Fig. 4.

Gas content versus depth and coal rank in the Black Warrior Basin, Alabama (McFall et al., 1986).

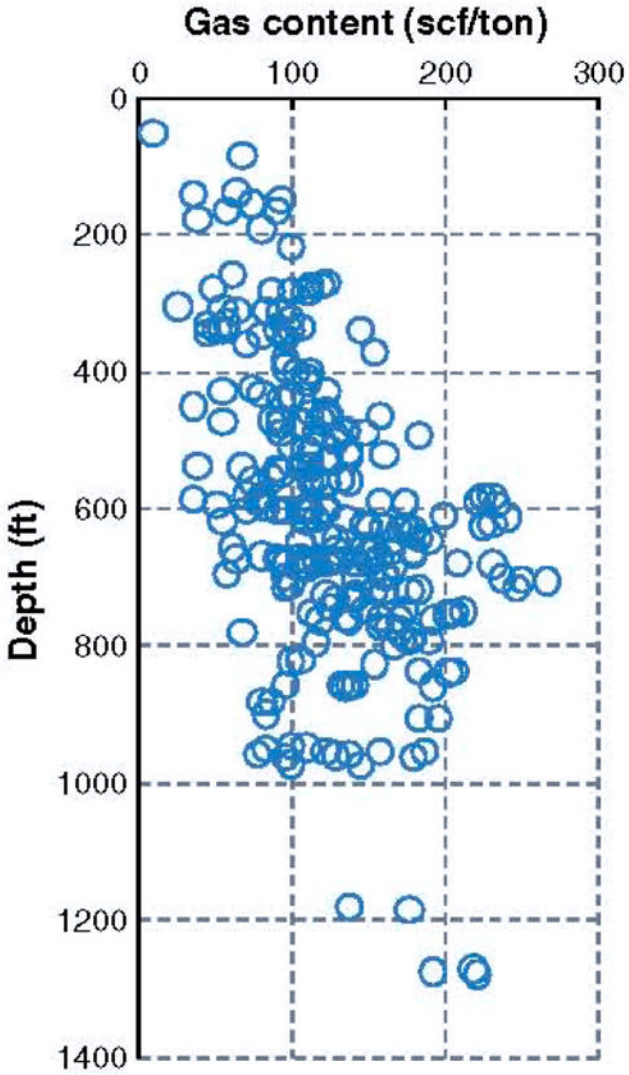

Fig. 5.
Total gas content-depth data of all coal beds within the interval of interest in the study area.

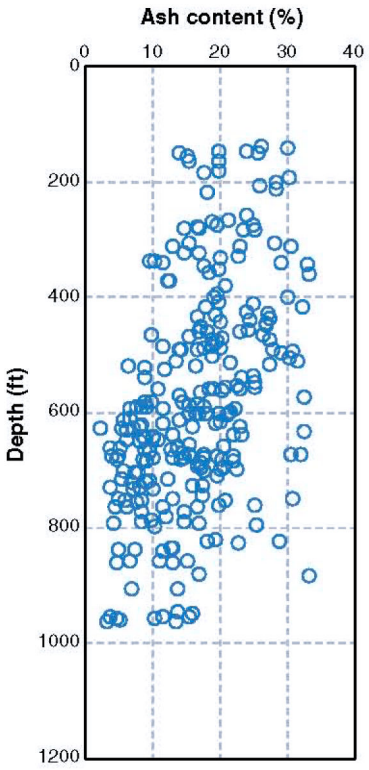

Fig. 6.
Ash content of the seams studied in this work as a function of depth.

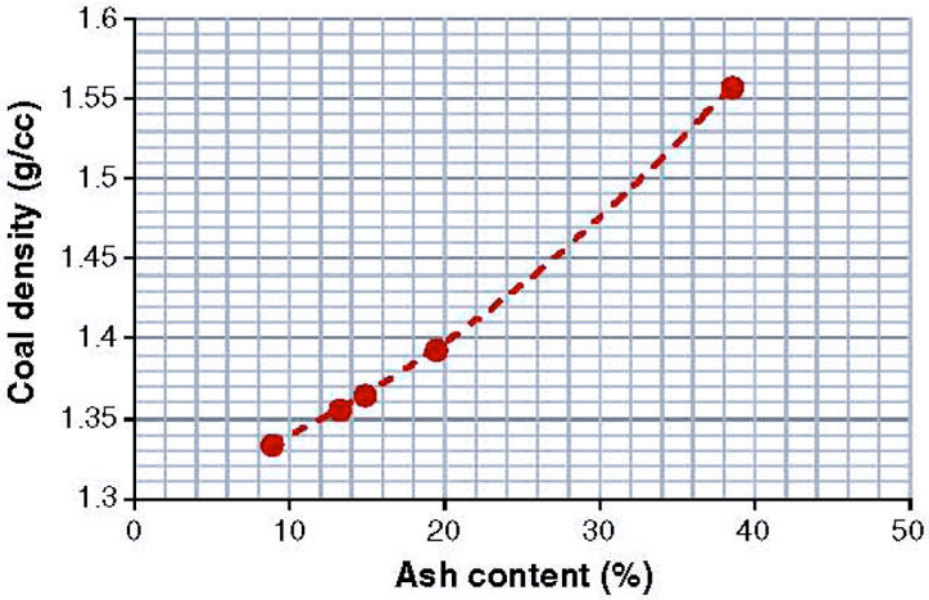

Fig. 7.

Ash content and bulk density relation established by data from the Pittsburgh, Pittsburgh rider, Redstone, Sewickley, and Waynesburg coals.

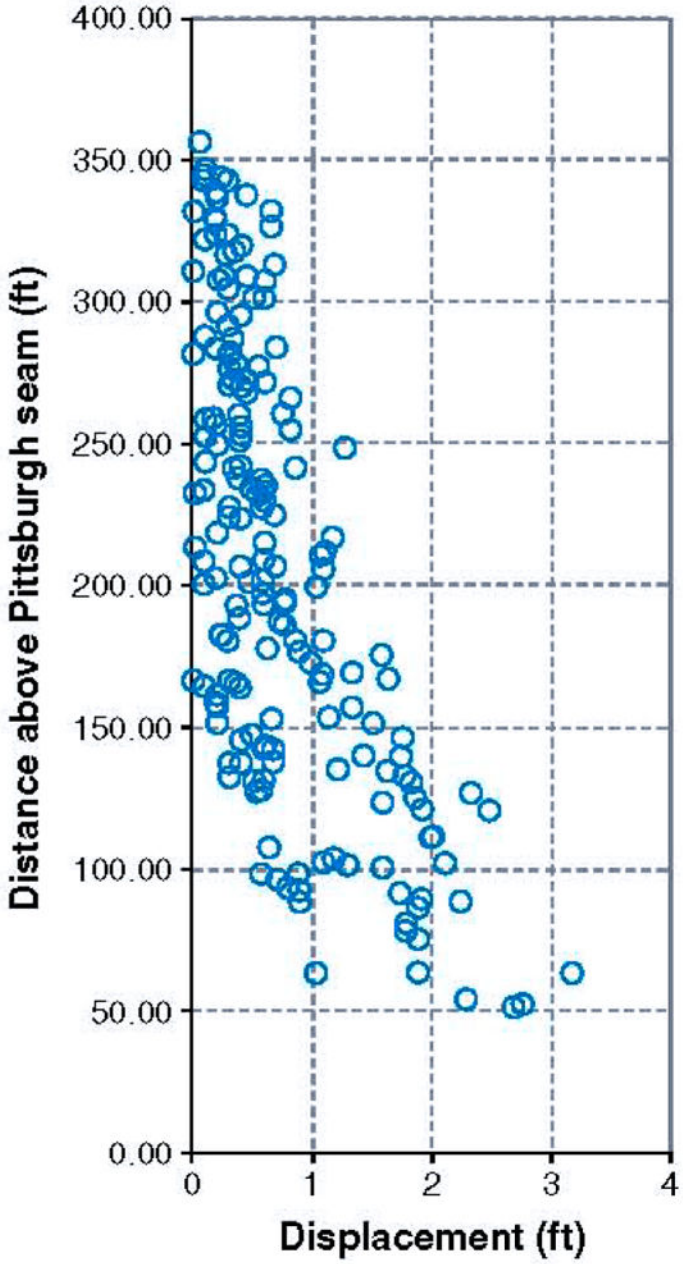

Fig. 8.

Strata displacements (exclusive of surface subsidence) measured in some gas capture boreholes drilled in the southwestern Pennsylvania section of the Northern Appalachian basin.

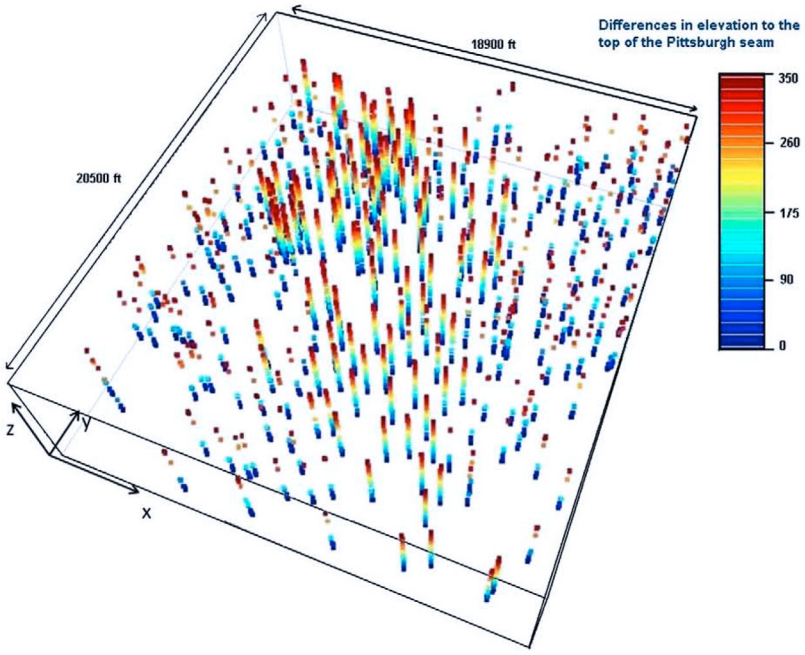

Fig. 9.

Spatial locations of the boreholes drilled over the area shown in Fig. 2 and differences in elevation for all identified formations above the top of the Pittsburgh seam. In this figure. “x” direction is Easting and “y” direction is Northing.

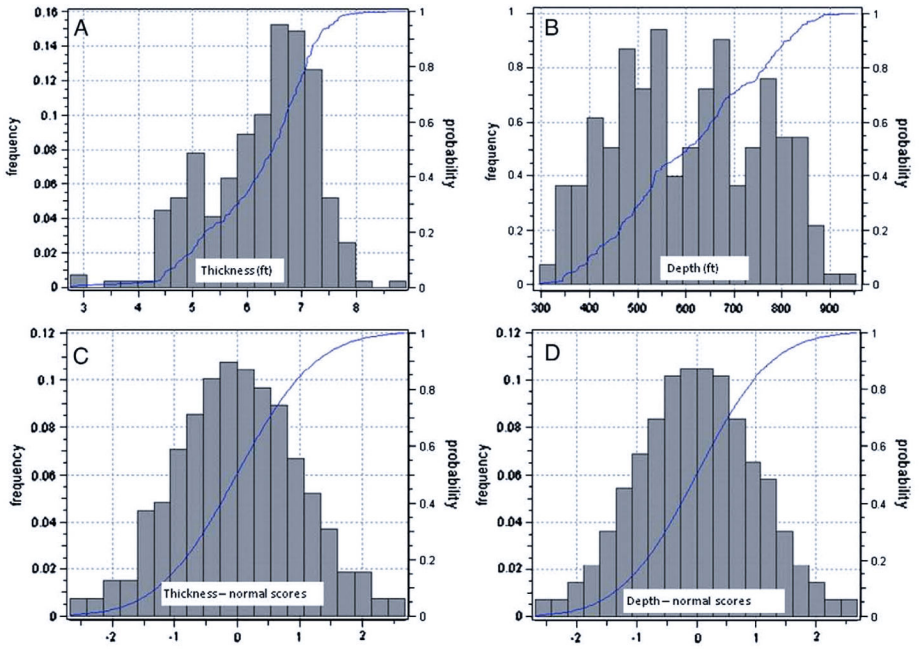

Fig. 10.

Frequency and cumulative frequency distribution of thickness data of Waynesburg coal (A) and depth of Sewickley coal (B), and normal-score transformation of these distributions (C and D).

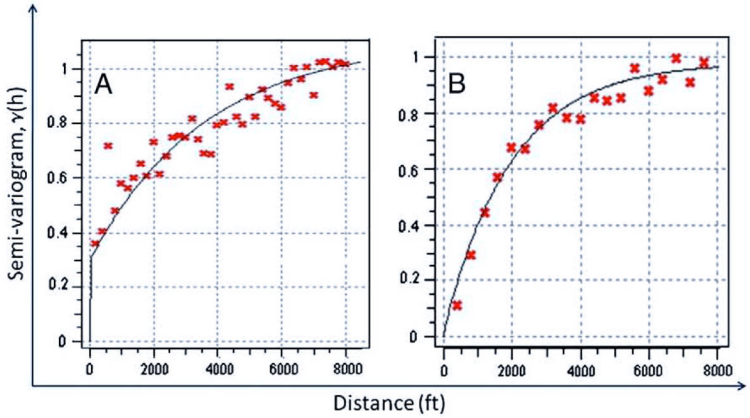

Fig. 11.

Example omni-directional experimental semivariograms of normal scores of WBC thickness (A) and SWC depth (B), and the analytical exponential semivariograms representing these.

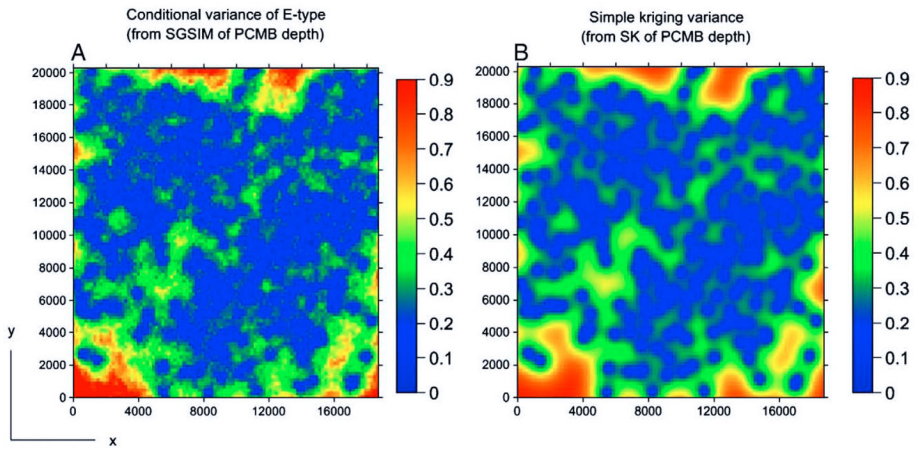

Fig. 12.

Variance maps obtained from SGSIM realizations (A) and simple kriging (B) of the Pittsburgh seam depth estimated in normal-score space.

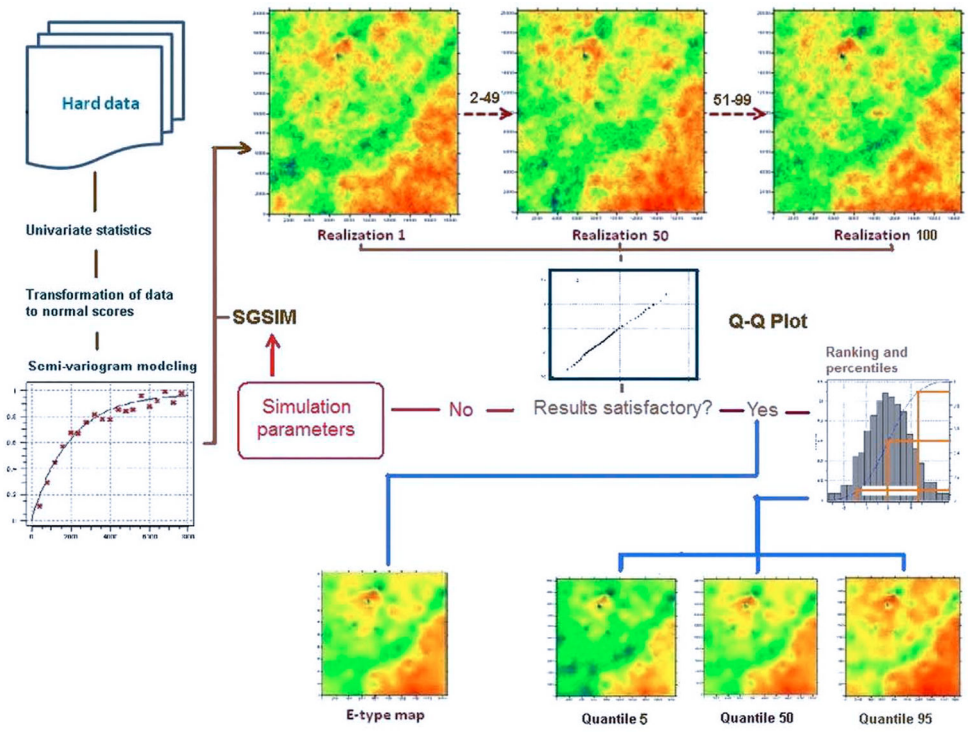

Fig. 13.

Schematic flow chart showing data generation and comparison of simulation results for the thickness of PCMB. The same flowchart of comparison and interpretation procedure was performed for each simulated attribute of each coal and non-coal layer after sequential simulations.

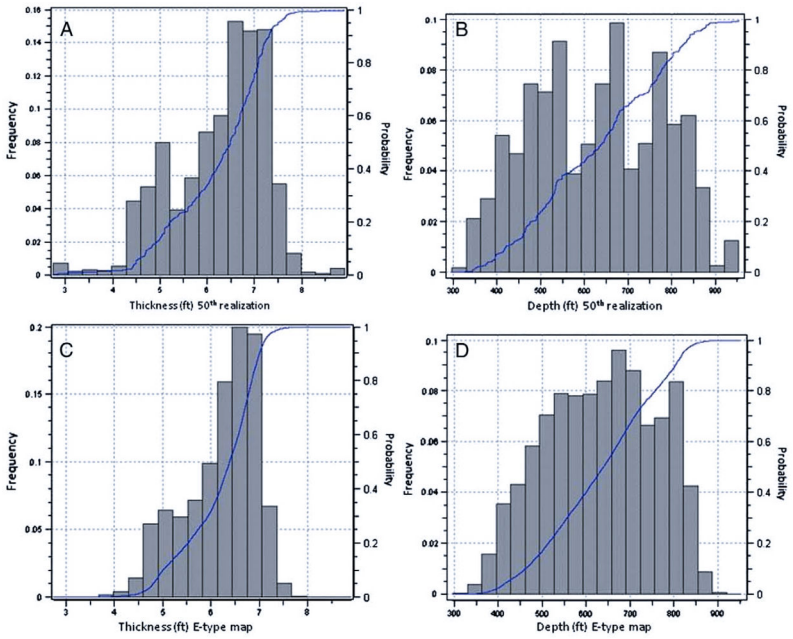

Fig. 14.

Frequency and cumulative frequency distributions of data from 50th realizations of SGSIM runs and E-type maps for thickness of Waynesburg coal (A and C) and depth of Sewickley coal (B and D). Histograms of hard data are shown in Fig. 10.

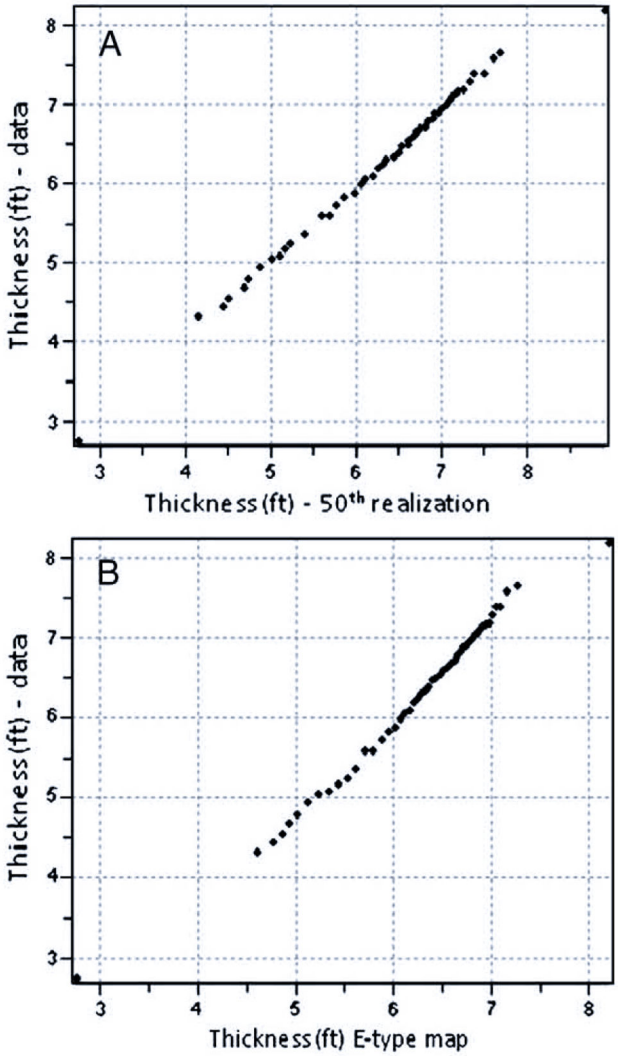

Fig. 15.
Q–Q plots of thickness of Waynesburg coal against the data of 50th realization from SGSIM (A) and E-type map (B).

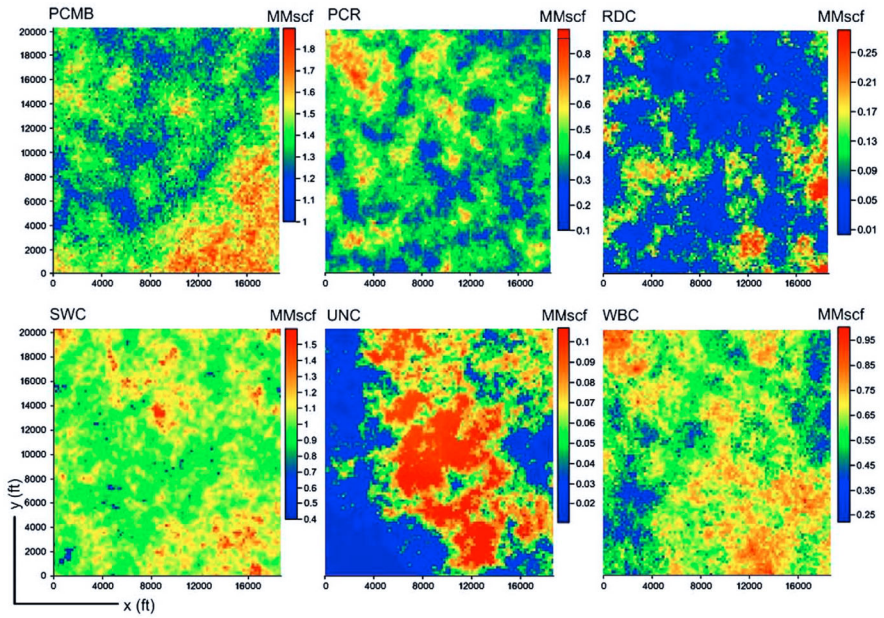

Fig. 16.
50th realization of in-place methane contents within the studied coals.

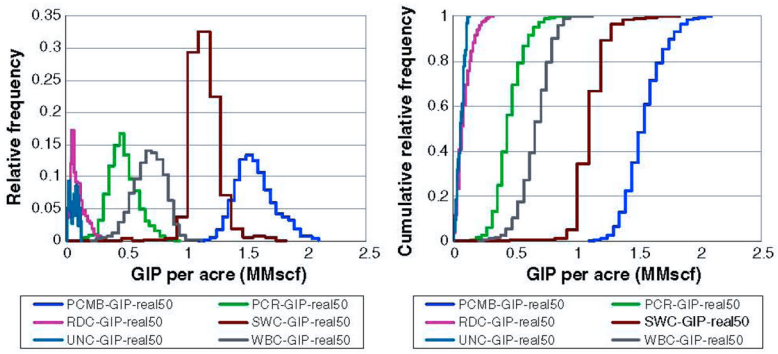

Fig. 17.
GIP-per-acre distributions of the realizations shown in Fig. 16.

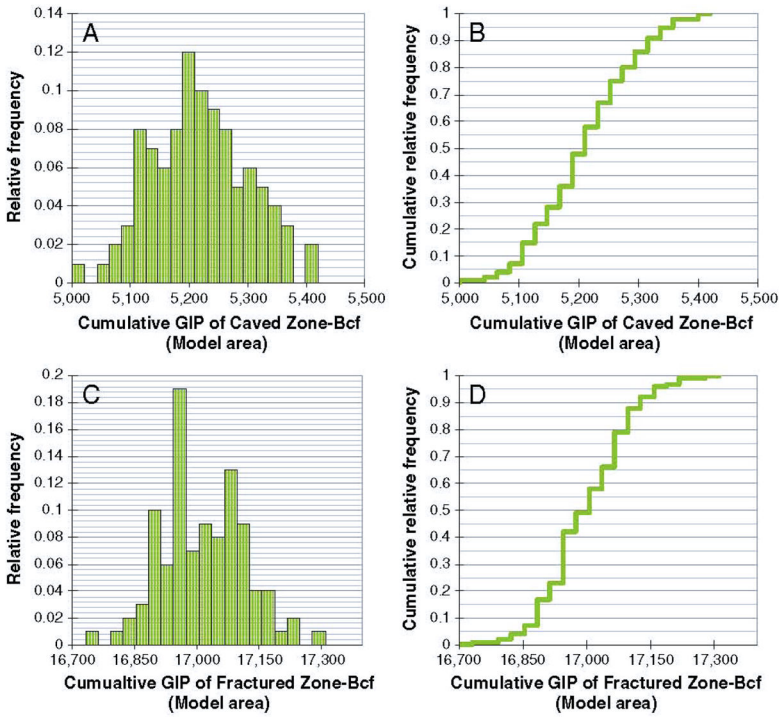

Fig. 18.

Relative frequency and cumulative relative frequency distributions of GIP amounts of 100 realizations computed for the caved zone (A and B) and fractured zone (C and D).

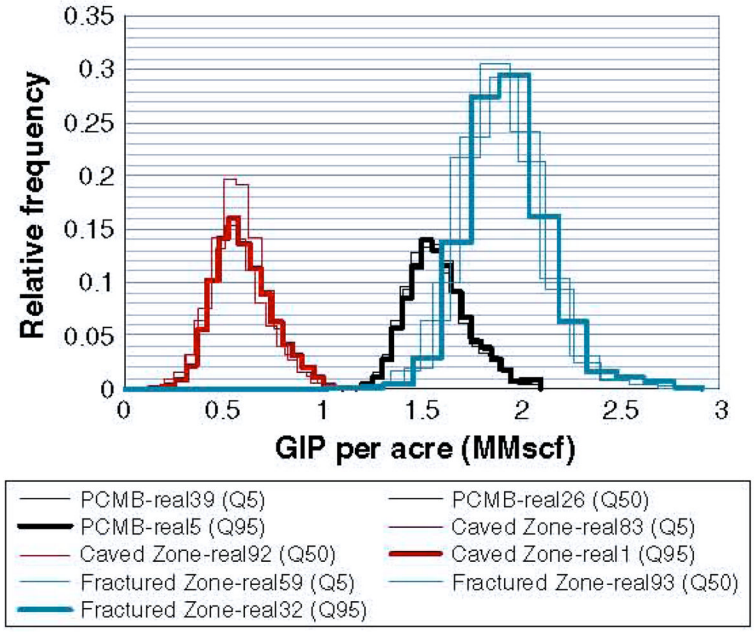

Fig. 19.

Distributions of gas-in-place estimations per acre of the PCMB, caved zone, and fractured zone at Q5, Q50, and Q95.

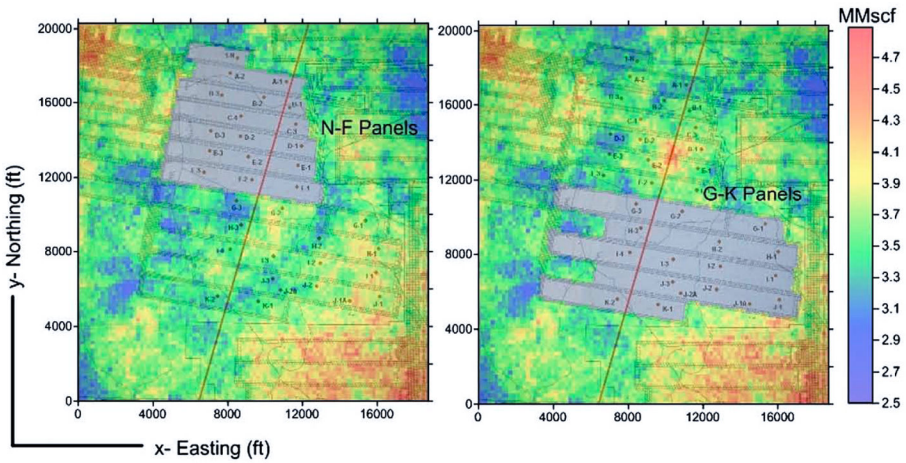

Fig. 20.

Panel series that were blanked within the model area to calculate GIP. The map in the background is the total GIP map of the PCMB + caved zone + fractured zone at Q50.

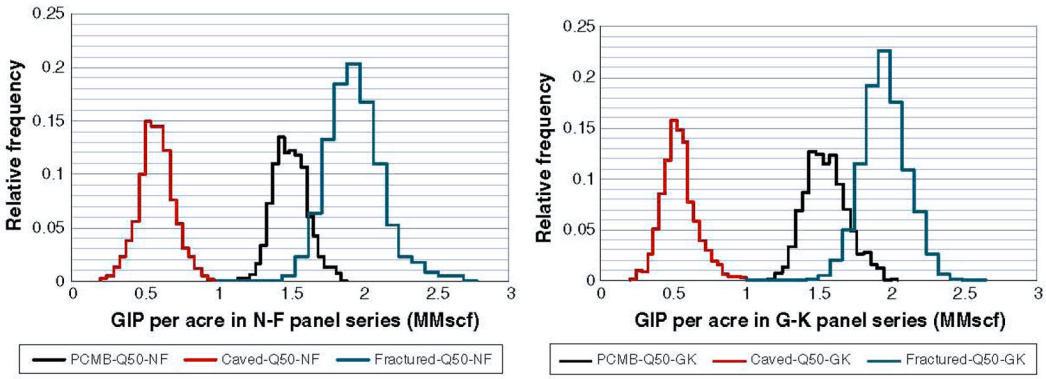

Fig. 21.

Distributions of GIP per acre in N–F and G–K panel series at Q50.

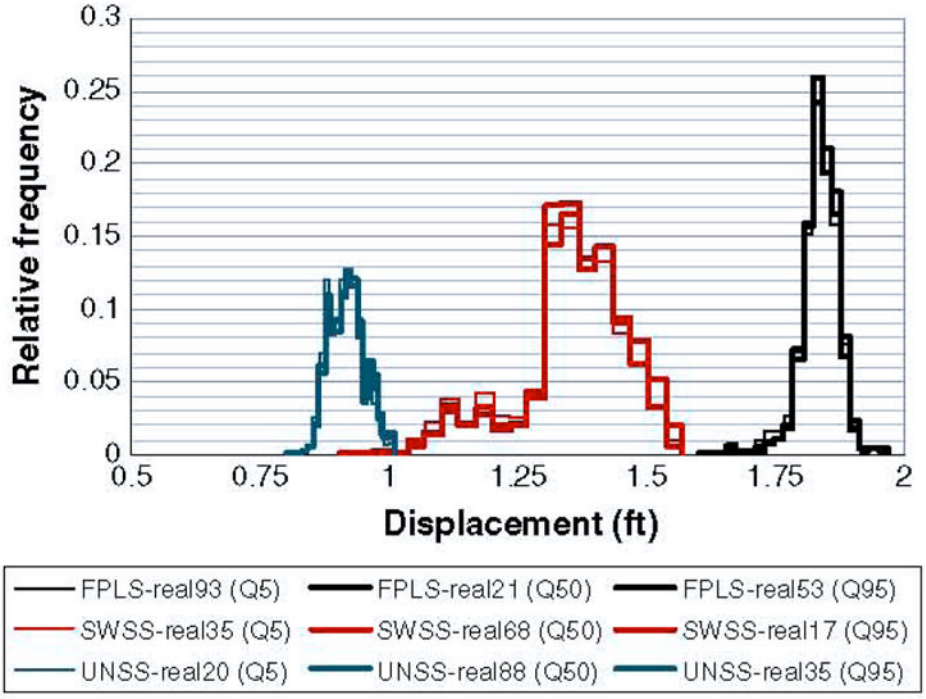

Fig. 22.

Displacement distributions of FPLS, SWSS, and UNSS over the entire model area at various quantiles and corresponding realizations.

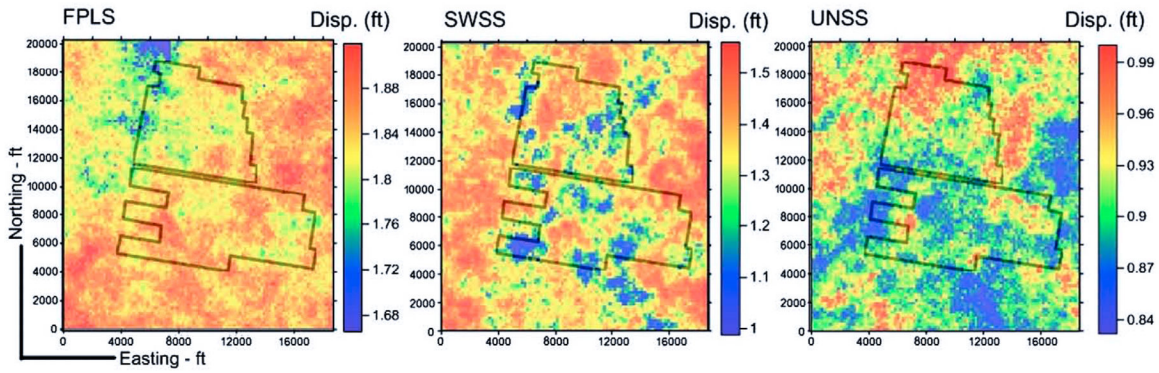

Fig. 23.

Displacement maps of FPLS, SWSS, and UNSS within the gas emission zone of the mining area shown in Fig. 2 at Q50. The locations of the N–F and G–K panel series are provided to correlate their positions with higher displacements.

Table 1

Mean (μ) and standard deviation (σ) of gas content (GC) of different coals and their overburden depth and the correlation coefficients (ρ) between variable pairs used in calculating joint probability distributions. The polynomial representations of gas content and depth relationships at 50Z coefficient of logistic functions (Q50) are also given. In these equations, “x” is the overburden depth.

Coal	Data pairs (means and standard deviations)		Correlation	Gas content (scf/ton) equations for Q50
	GC (scf/ton)	Overburden (ft)		
PCMB	μ= 167.8 σ = 47.9	μ=697.1 σ= 139.9	ρ = 0.257	$-6E\text{-}05x^2+0.1416x+95.685$
PCR	μ= 130.5 σ = 37.2	μ = 612.7 σ= 144.8	ρ = 0.619	$-9E\text{-}05x^2+0.2124x+18.654$
RDC	μ= 115.75 σ = 34.2	μ = 590.6 σ= 143.8	ρ = 0.558	$-7E\text{-}05x^2+0.1765x+25.120$
SWC	μ= 142.3 σ = 24.4	μ = 644.2 σ= 145.6	ρ=0.151	$-3E\text{-}05x^2+0.0501x+120.590$
UNC	μ = 96.2 σ = 22.3	μ = 478.6 σ= 169.5	ρ = 0.143	$-1E\text{-}05x^2+0.027x+88.285$
WBC	μ = 93.8 σ = 27.1	μ = 483.3 σ= 169.6	ρ = 0.415	$-4E\text{-}05x^2+0.0779x+57.736$

Table 2

Results of Monte Carlo simulations to determine the relationship of gas content (GC) and depth for Q5 and Q95 for studied coals. The values of gas contents with the standard error of MC simulations are also given in this table. In these equations, "x" is the overburden depth.

Coal	Gas content (scf/ton) at Q5 and Q95 and the standard errors of MC simulations[a]				Gas content (scf/ton) equations for Q5 and Q95 as a result of Monte Carlo simulations[a]	
	Q5		Q95		Q5	Q95
	GC	Std. err.	GC	Std. err.		
PCMB	90.9	0.0336	239.5	0.0908	$-6E\text{-}05x^2+0.1155x+40.685$	$-6.5E\text{-}05x^2+0.1816x+145.685$
PCR	69.9	0.0648	165.1	0.1529	$-6E\text{-}05+0.1356x+10.654$	$-11E\text{-}05x^2+0.2824x+35.654$
RDC	71.8	0.0629	140.4	0.1381	$-7E\text{-}05x^2+0.1427x+13.575$	$-1E\text{-}04x^2+0.2524x+28.287$
SWC	99.7	0.0018	187.1	0.0265	$-1E\text{-}06x^2+0.0031x+98.100$	$-4E\text{-}05x^2+0.07595x+155.590$
UNC	59.7	0.0187	127.5	0.0259	$-1E\text{-}05x^2+0.025x+50.285$	$-1E\text{-}05x^2+0.0310x+115.285$
WBC	45.4	0.0356	133.6	0.0902	$-3E\text{-}05*x^2+0.0579x+25.256$	$-6E\text{-}05x^2+0.1316x+85.750$

[a]Monte Carlo simulation results are based on 20,000 runs.

Table 3

Mean (μ) and standard deviation (σ) of ash content of different coals, their overburden depth, and the correlation coefficients (ρ) between variable pairs used in calculating joint probability distributions. The polynomial representations of ash content and depth relationships at 50% coefficient of logistic functions (Q50) are also given. In these equations, “x” is the overburden depth.

Coal	Data pairs (means and standard deviations)		Correlation	Ash content (%) equations for Q50
	Ash content (%)	Overburden (ft)		
PCMB	μ = 7.78 σ = 3.03	μ= 702.98 σ= 195.72	ρ = −0.0045	$9E\text{-}07x^2-0.0021x+9.046$
PCR	μ = 19.55 σ= 6.86	μ= 609.58 σ= 142.42	ρ = −0.1220	$4E\text{-}06x^2-0.0076x+24.06$
RDC	μ= 18.38 σ=7.41	μ= 710.80 σ=326.24	ρ = −0.3210	$8E\text{-}06x^2-0.0165x+25.118$
SWC	μ= 12.00 σ = 3.18	μ= 674.72 σ = 168.78	ρ = −0.2610	$3E\text{-}06x^2-0.007x+16.258$
UNC	μ= 22.72 σ = 5.39	μ= 468.46 σ = 160.94	ρ = − 0.0647	$3E\text{-}06x^2-0.0095x+25.010$
WBC	μ= 19.62 σ = 4.74	μ= 526.38 σ= 204.21	ρ= −0.1760	$8E\text{-}07x^2-0.0052x+22.038$

Table 4

Results of Monte Carlo simulations to determine the relationship of ash content and depth for Q5 and Q95 for studied coals. The values of ash contents with the standard error of MC simulations are also given in this table. In these equations, "x" is the overburden depth.

Coal	Ash (%) at Q5 and Q95 and the standard errors of MC simulations[a]				Ash content (%) equations for Q5 and Q95 as a result of Monte Carlo simulations[a]	
	Q5		Q95		Q5	Q95
	Ash	Std. err.	Ash	Std. err.		
PCMB	4.03	0.0019	11.70	0.0011	4.0E-7x^2−0.0019x+5.1694	1.2E-6x^2−0.0024x+12.7983
PCR	8.26	0.0049	32.14	0.0022	2.55E-06x^2−0.0079x+12.15	4.2E-6x^2−0.0072*x+34.965
RDC	8.58	0.0128	26.19	0.0156	7E-06x^2−0.0145x+15.345	9E-06x^2−0.0182x+34.578
SWC	6.31	0.0049	17.90	0.0028	2.5E-06x^2−0.0074x+10.169	3.5E-06x^2−0.0069x+20.965
UNC	13.28	0.0063	29.65	0.0077	2.0E-06x^2−0.0075x+16.456	4E-06x^2−0.0106x+33.865
WBC	11.55	0.0036	27.38	0.0080	7.0E-07x^2−0.0032x+13.045	9.0E-07x^2−0.0065x+30.550

[a]Monte Carlo simulation results are based on 20,000 runs.

Table 5

Mean (μ) and standard deviation (σ) of displacement and distance from the Pittsburgh coal bed and the correlation coefficients (ρ) between variable pairs used in calculating joint probability distributions. The polynomial expression relating displacement and distance to mined seam at a 50% coefficient of logistic function (Q50) is given in the bottom row.

Data pairs		Correlation
Displacement (ft)	Distance from coal bed (ft)	ρ = −0.676
μ = 0.746	μ = 205.22	
σ = 0.638	σ = 79.367	

Displacement (ft) = $0.000008*x^2 - 0.0063*x + 2.0439$, where x is distance above mined coal bed.

Int J Coal Geol. Author manuscript; available in PMC 2015 September 30.

Table 6

Univariate statistical parameters of depth, thickness, and gas content for PCMB, PCR, RDC, SWC, UNC, and WBC.

	Pittsburgh (PCMB)	Pitts. Riders (PCR)	Redstone (RDC)	Sewickley (SWC)	Uniontown Coal (UNC)	Waynesburg (WBC)
Depth (ft)						
Data	272	255	101	276	30	269
Maximum	1042.25	1033.44	998.17	952.67	725.80	709.61
U. quartile	834.06	828.96	753.40	738.22	633.75	503.50
Median	690.75	681.63	619.10	602.58	514.50	358.40
L quartile	577.82	570.06	545.68	486.52	363.10	273.74
Minimum	414.4	404.96	388.65	296.85	190.90	84.58
Mean	697.94	690.11	649.48	604.69	495.19	366.46
Variance	22,318.90	22,297.40	19,528.20	22,619.50	30,433.10	22,332.5
Thickness (ft)						
Data	272	247	98	272	30	269
Maximum	7.75	4.90	1.70	8.42	0.84	8.90
U. quartile	6.53	3.22	0.91	6.00	0.42	7.00
Median	6.25	2.80	0.60	5.65	0.25	6.48
L quartile	6.00	2.40	0.35	5.33	0.20	5.60
Minimum	5.05	0.96	0.03	2.40	0.10	2.75
Mean	6.28	2.83	0.67	5.69	0.33	6.25
Variance	0.19	0.54	0.15	0.34	0.04	0.96
Gas cont–Q50 (scf/ton)						
Data	272	255	101	276	30	269
Maximum	125.26	125.12	124.30	122.95	111.44	110.36
U. quartile	117.84	117.57	113.21	112.25	104.94	94.45
Median	109.07	108.43	103.83	102.55	95.38	81.57
L quartile	100.60	99.97	97.88	92.99	82.00	70.97
Minimum	86.65	85.80	84.32	75.85	66.07	56.36
Mean	108.36	107.83	105.15	101.74	92.92	81.98
Variance	99.65	102.79	97.59	130.02	220.41	178.47

Table 7

Univariate statistical parameters of overburden depth and displacement (Q50) of non-coal intervals.

	Fishpot limestone (FPLS)	Sewickley sandstone (SWSS)	Uniontown sandstone (UNSS)
Depth (ft)			
Number of data	212	214	189
Maximum	1017.83	940.50	776.42
Upper quartile	779.75	737.5	564.05
Median	655.60	596.08	421.80
Lower quartile	542.00	492.15	310.70
Minimum	394.20	247.68	141.63
Mean	662.79	600.92	429.61
Variance	21,595.10	23,384.50	21,343.00
Displacement (ft)–Q50			
Number of data	212	214	189
Maximum	1.96	1.56	1.00
Upper quartile	1.86	1.43	0.93
Median	1.84	1.36	0.91
Lower quartile	1.82	1.31	0.89
Minimum	1.67	0.99	0.84
Mean	1.84	1.35	0.92
Variance	0.001	0.013	0.001

Table 8

Summary of parameters that describe analytical semivariograms for depth, thickness and gas content (Q50) attributes of PCMB, PCR, RDC SWC, UNC and WBC. All semivariograms were analyzed using normal-score data and were described with one nested structure (model).

	Pittsburgh (PCMB)	**Pitts. Riders (PCR)**	**Redstone (RDC)**	**sewickley (SWC)**	**uniontown coal (UNC)**	**Waynesburg (WBC)**
Depth (ft)						
Model	Spherical	Spherical	Spherical	Exponential	Gaussian	Exponential
Nugget	0.02	0.05	0.20	0.05	0.05	0.02
Sill	0.83	0.80	0.80	0.90	0.95	0.93
Maximum range	3402	4032	8200	5396	8125	5775
Medium range	3160	3830	8000	5168	7875	5700
Minimum range	3078	3763	7700	4940	7250	5550
Thickness (ft)						
Model	Exponential	Spherical	Spherical	Exponential	Exponential	Exponential
Nugget	0.40	0.02	0.10	0.01	0.01	0.30
Sill	0.60	0.90	0.90	0.80	0.8	0.70
Maximum range	9750	2420	2220	1872	8250	7600
Medium range	9500	2156	2160	1836	8125	7280
Minimum range	9250	2112	2040	1728	7875	7200
Gas cont–Q50 (scf/ton)						
Model	Exponential	Exponential	Exponential	Exponential	Gaussian	Exponential
Nugget	0.01	0.05	0.15	0.02	0.01	0.05
Sill	0.87	0.84	0.85	0.97	0.99	0.90
Maximum range	4473	5103	9765	6834	6875	6000
Medium range	4347	4977	9555	6528	6375	5850
Minimum range	4158	4788	9345	6120	6250	5700

Table 9

Summary of parameters that describe analytical semivariograms for depth and displacement of FPLS, SWSS, and UNSS. All semivariograms were analyzed using normal-score data.

	Fishpot limestone (FPLS)	Sewickley sandstone (SWSS)	Uniontown sandstone (UNSS)
Depth (ft)			
Model	Gaussian	Spherical	Spherical
Nugget	0.08	0.05	0.10
Sill	0.78	0.80	0.85
Maximum range	3116	4100	4640
Medium range	2812	4035	4320
Minimum range	2736	4000	4160
Displacement (ft)–Q50			
Model	Exponential	Exponential	Exponential
Nugget	0.10	0.01	0.10
Sill	0.70	1.00	0.90
Maximum range	6075	5200	5300
Medium range	6000	4900	5100
Minimum range	5925	4700	4900

Table 10

Basic statistical measures of the GIP amounts derived from distributions shown in Fig. 17.

Variable	# of cells	Min. (MMscf)	Max. (MMscf)	Mean (MMscf)	Std. dev.
PCMB–GIP–real50	10,000	1.143	2.095	1.575	0.161
PCR–GIP–real50	10,000	0.129	0.942	0.478	0.117
RDC–GIP–real50	10,000	0.003	0.316	0.096	0.062
SWC–GIP–real50	10,000	0.464	1.739	1.157	0.122
UNC–GIP–real50	10,000	0.012	0.120	0.063	0.032
WBC–GIP–real50	10,000	0.247	1.127	0.693	0.128

Table 11

Q5, Q50, and Q95 for cumulative GIP in the model area, average GIP per acre, and corresponding realizations for all coal seams.

Coal seam	Q5			Q50			Q95		
	Cum. GIP (Bcf)	GIP per acre (MMscf)	Real. seq. #	Cum. GIP (Bcf)	GIP per acre (MMscf)	Real. seq. #	Cum. GIP (Bcf)	GIP per acre (MMscf)	Real. seq. #
PCMB	13.962	1.569	39	14.040	1.578	26	14.133	1.588	5
PCR	4.239	0.476	82	4.328	0.486	81	4.432	0.498	46
RDC	0.811	0.091	26	0.885	0.099	27	0.981	0.110	59
SWC	10.238	1.150	33	10.327	1.160	75	10.403	1.169	80
UNC	0.415	0.047	37	0.504	0.057	45	0.572	0.064	12
WBC	6.124	0.688	86	6.191	0.696	38	6.264	0.704	84

Table 12

Cumulative GIP for the caved zone and fractured zone at Q5, Q50, and Q95, and the corresponding realizations.

Zone	Q5		Q50		Q95	
	Cum. GIP (Bcf)	Real. seq. #	Cum. GIP (Bcf)	Real. seq. #	Cum. GIP (Bcf)	Real. seq. #
Caved	5.093	83	5.213	92	5.351	1
Fractured	16.854	59	17.011	93	17.174	32

Table 13

Gas-in-place amounts that are estimated per acre for different sections of the gas emission zone at Q5, Q50, and Q95 derived from the GIP distributions given in Fig. 19 of their corresponding realizations.

Coal/zone/realization/quantile	# of cells	Min. (MMscf)	Max. (MMscf)	Mean (MMscf)	Std. dev.
PCMB–real39 (Q5)	10,000	1.149	2.080	1.569	0.150
PCMB–real26 (Q50)	10,000	1.104	2.093	1.578	0.155
PCMB–real5 (Q95)	10,000	1.138	2.091	1.588	0.160
Caved zone–real83 (Q5)	10,000	0.174	1.128	0.572	0.149
Caved zone–real92 (Q50)	10,000	0.152	1.153	0.586	0.136
Caved zone–real1 (Q95)	10,000	0.189	1.160	0.601	0.146
Fractured zone–real59 (Q5)	10,000	0.828	2.888	1.894	0.205
Fractured zone–real93 (Q50)	10,000	0.933	2.731	1.911	0.199
Fractured zone–real32 (Q95)	10,000	0.849	2.814	1.930	0.203

Table 14

Cumulative gas-in-place amounts within the PCMB, caved zone, and fractured zone of N-F and G-K panel areas corresponding to the Q50 quantile.

Zones/quantile/panels	Cumulative GIP (Bcf)
PCMB-Q50-GK	2.508
PCMB-Q50-NF	1.821
Caved-Q50-GK	0.873
Caved-Q50-NF	0.705
Fractured-Q50-GK	3.156
Fractured-Q50-NF	2.354

Table 15

GIP amounts that are estimated per acre of mining for different sections of the gas emission zone within N-F and G-K panel series at Q50. These statistics are derived from the distributions given in Fig. 21.

Zone/quantile/panels	# of cells	Min. (MMscf)	Max. (MMscf)	Mean (MMscf)	Std. dev.
PCMB-Q50-NF	1364	1.160	1.885	1.502	0.116
Caved-Q50-NF	1364	0.206	1.053	0.582	0.120
Fractured-Q50-NF	1364	1.146	2.679	1.942	0.188
PCMB-Q50-GK	1823	1.139	2.034	1.547	0.145
Caved-Q50-GK	1823	0.230	0.984	0.539	0.119
Fractured-Q50-GK	1823	1.128	2.542	1.947	0.154

Table 16

Basic statistical attributes of rock strata displacement distributions shown in Fig. 22.

Rock/realization/quantile	# of cells	Min. (ft)	Max. (ft)	Mean (ft)	Std. dev.
FPLS-real93 (Q5)	10,000	1.666	1.961	1.834	0.039
FPLS-real21 (Q50)	10,000	1.666	1.963	1.838	0.035
FPLS-real53 (Q95)	10,000	1.666	1.963	1.840	0.033
SWSS-real35 (Q5)	10,000	0.986	1.564	1.344	0.111
SWSS-real68 (Q50)	10,000	0.987	1.561	1.354	0.100
SWSS-real17 (Q95)	10,000	0.989	1.565	1.364	0.106
UNSS-real20 (Q5)	10,000	0.833	1.009	0.914	0.032
UNSS-real88 (Q50)	10,000	0.832	1.010	0.917	0.034
UNSS-real35 (Q95)	10,000	0.834	1.010	0.921	0.035

Conversion table (English to SI units)

1 acre	4046.85 m^2
1 ft	0.3048 m
1 MMscf	28,316 m^3
1 scfm	0.0004719 m^3/s
1 scfd	0.6795 m^3/day